Delft University of Technology

Effect of Wing Stiffness and Folding Wingtip Release Threshold on Gust Loads

Carrillo Córcoles, X.; Mertens, C.; Sciacchitano, A.; van Oudheusden, B.W.; De Breuker, R.; Sodja, J.

Important note
To cite this publication, please use the final published version (if applicable).
Please check the document version above.

Effect of Wing Stiffness and Folding Wingtip Release Threshold on Gust Loads

Xavier Carrillo Córcoles,* Christoph Mertens,† Andrea Sciacchitano,‡
Bas W. van Oudheusden,§ Roeland De Breuker,¶ and Jurij Sodja**
Delft University of Technology, 2629 HS Delft, The Netherlands

This study presents an aeroelastic wind-tunnel experiment to identify the influence of the wing stiffness and hinge release threshold on the gust load alleviation performance of a folding wingtip design. Five models with different stiffness and tailoring properties are tested, and the wing root bending moment at different conditions is compared to the response with the locked-hinge condition to assess the impact on the gust load alleviation capabilities of the folding wingtip. The results show that the structural properties do not have an important impact on the peak load alleviation but the hinge release threshold and timing do. Releasing with the correct timing can reduce significantly the peak loads. However, the dynamics of the system are affected by this release; the flutter speed is decreased, and, although the performance can improve, load oscillations increase, which can be considered detrimental for reasons such as fatigue or passenger comfort.

Nomenclature

B = full wing semispan, m
b = main wing semispan, m
C_B = bending moment coefficient
$\bar{C}$ = stiffness calibration matrix, (N · m)/V
c = wing chord, m
$\bar{c}$ = compliance calibration matrix, V/(N · m)
$\tilde{D}_{11}$ = bending modulus of elasticity, N · m
$\tilde{E}_{11}$ = engineering modulus of elasticity, N/m
G = bridge signals, V
g = damping coefficient
M_S = torque in classical laminate plate theory, N · m
M_X = bending moment in classical laminate plate theory, N · m
n = number of design variables (plies)
S = wing surface, m²
t = laminate thickness, m
U = airspeed, m/s
α = angle of attack, deg
β = fold angle, deg
γ = ply angle misalignment, deg
ε_i = threshold for ith constrain of optimization problem
θ = ply angle, deg
Λ = flare angle, deg
ρ = air density, kg/m³

*Researcher, Faculty of Aerospace Engineering, Aerospace Structures and Computational Mechanics, Kluyverweg 1; X.CarrilloCorcoles@tudelft.nl.

†Ph.D. Candidate, Faculty of Aerospace Engineering, Aerodynamics, Kluyverweg 2; C.Mertens@tudelft.nl.

‡Associate Professor, Faculty of Aerospace Engineering, Aerodynamics, Kluyverweg 2; A.Sciacchitano@tudelft.nl.

§Associate Professor, Faculty of Aerospace Engineering, Aerodynamics, Kluyverweg 2; B.W.vanOudheusden@tudelft.nl.

¶Associate Professor, Faculty of Aerospace Engineering, Aerospace Structures and Computational Mechanics, Kluyverweg 1; R.deBreuker@tudelft.nl. Associate Fellow AIAA.

**Associate Professor, Faculty of Aerospace Engineering, Aerospace Structures and Computational Mechanics, Kluyverweg 1; J.Sodja@tudelft.nl. Senior Member AIAA.

I. Introduction

AIRCRAFT aerodynamic efficiency can be improved by increasing the wingspan and thereby the aspect ratio of the main wing [1]. However, increasing the wingspan can lead to increased structural weight of the wing due to increased structural loads in the inboard section of the wing, reduced handling qualities due to reduced roll rate, and operational difficulties due to limited parking space at the airports.

To address the operational difficulties, Boeing [2] implemented a folding wingtip (FWT) on the 777X, which can be folded when the airplane is on the ground and deployed before takeoff. On the other hand, Wilson et al. [3] proposed a FWT using a flared hinge, which can be released in flight, to address also the structural and handling drawbacks due to the span increase of the wing.

The numerical analyses presented by Castrichini et al. [4] showed that the FWT can reduce the wing root bending moment (WRBM) and provide a means of gust load alleviation (GLA). These results were confirmed in wind-tunnel tests. Cheung et al. [5,6] showed the potential for passive load alleviation of the system, achieving peak load reductions between 30 and 60%, and studied the active control of the FWT, which, depending on the timing of the actuation with respect to the gusts, can increase the GLA performance up to 80% reduction. In addition, this timing issue is also important when releasing the hinge because the release instant affects the magnitude of the load alleviation, as reported by Castrichini et al. [7,8].

Regarding the handling qualities, first Dussart et al. [9] and Castrichini et al. [10] in numerical analyses and later Healy et al. [11] in wind-tunnel tests found that it is possible to decrease the reduction of steady roll rates caused by the increment of the wingspan when the FWT is released. It is possible to achieve between 60 and 80% of the roll rate of a wing without wingtip extension.

To validate these findings in flight, Wilson et al. [12] used a scaled aircraft model based on the Airbus A321, the AlbatrossONE, that includes a hinge mechanism to lock and release the FWT. The results confirmed the potential of the concept for load alleviation, with load reductions between 20 and 40% depending on the FWT span, and presented the proof of concept with a gate-to-gate demonstration.

In continuation of their work, the current study proposes an aeroelastic experimental investigation to characterize how the load alleviation capabilities of the FWT are affected by the variation of the wing stiffness, passive load alleviation using composite tailoring, and the variation of the load threshold for releasing the hinge. Thanks to the introduction of composites, it is possible to manufacture lighter yet more flexible wings and introduce the concept of aeroelastic tailoring, which can be used to optimize the structural response of the wing during maneuvers and gust encounters [13]. Therefore, the
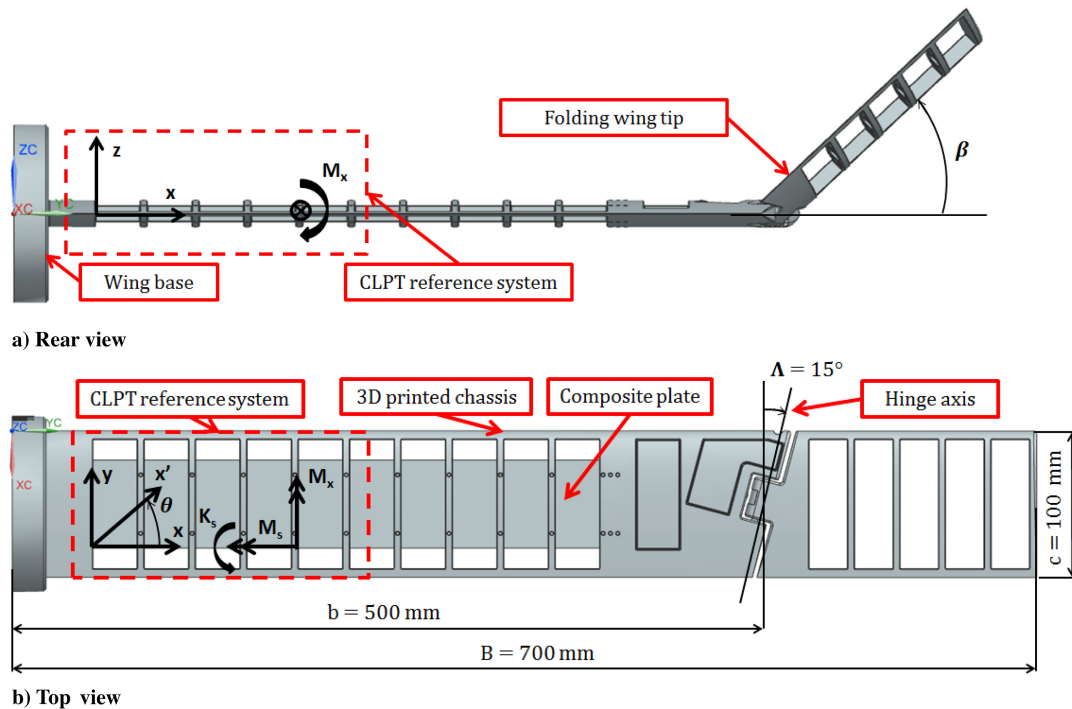
Fig. 1   CAD representation of the wind tunnel model without skin with an overview of its dimensions.

stiffness and bend/twist coupling properties of the main wing are varied to investigate their effect on the FWT alleviation performance.

Finally, given the importance of the hinge release timing shown by Castrichini et al. [7,8], the third parameter that is varied is the load threshold to release the FWT. This variation allows, on the one hand, studying experimentally what was observed in the mentioned numerical investigations and, on the other hand, in combination with the previous parameters, studying how the optimal threshold is affected by the structural properties of the main wing.

II.   Wing Design Study

The procedure and methodologies used to design the wind-tunnel model are addressed in this section. First, the characteristics of the wing are presented. Then, the finite element model used for sizing the experiment is explained. Next, the design and selection of the wing structure are defined. Finally, the simulations carried out for the sizing are presented.

A.   Wind-Tunnel Wing Model

The objective of this study is to establish the relationship between the stiffness properties of the main wing, the load threshold for the hinge release, and the GLA performance of the FWT. For this reason, the wind-tunnel model must fulfill two main requirements:

1) It must allow for a controlled variation of the structural properties.

2) It must include a mechanism to release the hinge based on the load threshold experienced by the wing.

In addition to the main functional requirements pertaining to the FWT, the model must allow the observation of aeroelastic effects pertinent to highly flexible wings (such as large deflections) in the wind tunnel. However, the deflections are constrained by the wind-tunnel cross-section, which constrains the size of the model and the magnitude of the structural deformations.

The model is designed as a rectangular half-wing with a chord c of 100 mm and a wing aspect ratio of 14 to maintain similar proportions as the AlbatrossONE [12] but simplifying the geometry to facilitate the parametric study. The main wing has a semispan b of 500 mm, and the wingtip extends the full semispan B to a total of 700 mm. In view of the restrictions set by the wing dimensions, a NACA 0018 airfoil is selected, to be able to fit the hinge mechanism inside the contour of

Table 1   Overview of model properties

Symbol	Description	Dimension
Λ, deg	Flare angle	15
B, mm	Full wing semispan	700
b, mm	Main wing semispan	500
c, mm	Chord	100
——	Airfoil	NACA 0018

the airfoil profile. Finally, the flare angle of the hinge Λ is set to 15 deg, as in the AlbatrossONE, and the wingtip fold angle is defined as β. The model and an overview of its dimensions are presented in Fig. 1 and Table 1.

With the objective of achieving large deflections at the given size of the model and easily varying the stiffness properties of the wing, the model is based on the Pazy wing concept proposed by Avin et al. [14]. It consists of a nylon PA12 three-dimensional (3D) printed chassis[††] covered with Oralight foil[‡‡] to provide the aerodynamic shape to the wing while a plate inside it acts as the primary structural element carrying the majority of the loads. Because the plate represents the primary load-bearing element of the wing, it is possible to effectively control the structural properties of the wing by only modifying the plate, whose bending stiffness and bend/twist coupling properties can be modified using composite tailoring, which is done with North Thin Ply Technology TP135 prepreg.[§§] The sizing of these plates is carried out using numerical simulations, explained in Sec. II.C.

Finally, the hinge has to be released at different instants of the gust response (depending on the set release load thresholds). Therefore, it is necessary to design a mechanism that can easily adapt the release time, achieve a short reaction time relative to the gust period, and

---

[††]See "PA2200 Product Information," EOS, 2001. https://cdn2.hubspot.net/hubfs/5154612/Material%20documentation/Nylon%20PA12/PA2200_Product_information_03-10_en.pdf [retrieved 28 July 2021].
[‡‡]See "Oralight," Lanitz-Prena Folien Factory, 2021, https://www.oracover.de/katalog/artikelinfo/4209/oralight-lightiron-on-film—width_-60-cm—length_-2-m [retrieved 28 July 2021].
[§§]See "TP135 Data Sheet," North Thin Ply Technology, 2019. https://www.thinplytechnology.com/assets/mesimages/NTPTTDS-TP135_V1-6.pdf [retrieved 28 July 2021].
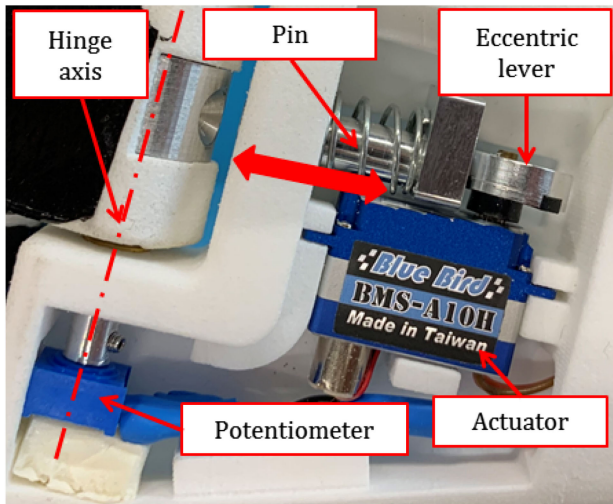
Fig. 2   Detail of the hinge mechanism in free-hinge condition.

operate consistently over the repetitions of the experiment. These requirements can be fulfilled by an active servoactuated mechanism, which simplifies the assembly and gives flexibility to the release possibilities.

The hinge release mechanism is designed to block the wingtip rotation by creating an interference between the main wing and the FWT. The realization of the mechanism is shown in Fig. 2. The locking pin is pressed against the hinge axle of the wingtip using an eccentric lever connected to a Blue Bird BMS-A10H rotary actuator,¶ which is controlled by an Arduino UNO microcontroller*** that releases the hinge at the desired instant. By adding a spring and a chamfer at the end of the pin, the system is designed in such a way that the FWT can start moving as soon as the pressure on the locking pin is released. This way, even if the pin has not moved to the end of its stroke, the FWT can already start to rotate. In addition, as a result of the axial alignment of the reaction force of the pin and the eccentric lever, the actuator does not have to actively resist the reaction load on the locking pin.

B.   Finite Element Model

The structural design of the wings, in particular the layup of the composite plates acting as the main load-bearing components, requires an assessment of the aeroelastic response to ensure that the desired aeroelastic phenomena can be observed in the wind tunnel. Therefore, the anticipated loads and deflections during the wind-tunnel test are studied by performing numerical simulations using Simcenter 3D [15] and MSc Nastran [16].

The structure of the wing is modeled using the approach presented by Avin et al. [14]. Figure 3 shows the FEM representation of the wing without skin. The leading and trailing edges are modeled as one-dimensional (1D) beams, while the ribs and the plate are modeled as (two-dimensional) 2D shells. For the ribs at end of the main wing, where there is no inner plate, ribs are modeled as a single surface. For the other ribs, only the D-shaped part at the leading edge and the rear triangle at the trailing edge are modeled and connected to each other with rectangular caps modeled as 1D beams. The glue bonding between the ribs and the plate is modeled using RBE2 1D elements. Finally, the wing skin is modeled as 2D shells.

In a simplification of the problem, Avin et al. [14] only modeled the skin when subjected to tensile loads, because buckling of the Oralight skin under compressive loads introduces nonlinearities to the analysis. However, both skins are modeled in this sizing study, as the oscillatory motion in the gust response makes both skins face compressive and tensional loads. The simulations are carried out with and without the skin to determine the upper and the lower envelopes of the

expected loads and deflections. The results without skin are considered conservative because, in the real structure, the skin would add to the stiffness of the structure and thereby also carry some of the loads. Similarly, the results including both the upper and the bottom skins are nonconservative, as the model becomes stiffer than the real structure when the buckling of the skin under compression is ignored. Hence, these results set a range in which the response of the physical wing can be expected.

The hinge is modeled following the approach proposed by Castrichini et al. [4]. The FE assembly of the hinge is shown in Fig. 4. The hinge is modeled using elastic CBUSH elements. RBE2 elements connect the wing and wingtip to the axis nodes, and the elastic elements connect both parts, as presented in Fig. 4. Figure 4a shows the FEM representation, and Fig. 4b presents a sketch of the different connections. When the hinge is released, the rotational degree of freedom (DOF) aligned with the hinge spring should be set to zero stiffness, allowing a free rotation. However, this approach leads to a statically underdetermined structure and, ultimately, numerical divergence. To avoid this numerical problem, the stiffness of the rotational DOF is set to relatively low stiffness, two orders of magnitude below the wing stiffness, hence making the spring act similarly to a hinge mechanism. The remaining DOF are set to relatively high stiffness values, two orders of magnitude above the wing stiffness, to model a rigid connection. On the other hand, when the wingtip is locked, the rotational DOF is also modeled as a rigid connection, hence limiting the rotation of the FWT.

Furthermore, the aeroelastic model is completed by coupling the aerodynamic model to the structural model of the wing. The doublet lattice method (DLM) is used to determine the aerodynamic forces acting on the wing. As shown by Cheung et al. [5], the DLM can only be applied to small deflections of the wingtip, and hence only the time up to the hinge release is studied. Because of the wind-tunnel setup, part of the wing has to be outside of the flow, so the aerodynamic mesh is only defined on the wingtip and the outboard part of the main wing, as seen in Fig. 3.

To conclude, ground vibration tests of the manufactured models are conducted to check the correlation with the numerical model and assess the level of discrepancy. This procedure of characterizing the structure and updating the numerical model can be found in Appendix A.

C.   Wing Spar Design

The wing spar in the form of a composite plate determines the main structural properties of the wing. For this study, five different plates are defined. The first three plates are designed with different bending stiffness to investigate how the wing bending stiffness affects the load alleviation performance of the FWT. Using one of these plates as a reference, two additional plates are designed with similar bending stiffness but including also the bend/twist coupling to provide wash-in and washout effects, which produce load enhancement and load alleviation effects, respectively. This way, the interaction between different aeroelastic tailoring objectives and the FWT can also be studied.

Special balanced laminates are used to vary the bending stiffness of the first three wings. This stacking sequence is antisymmetric about the midplane, and each half is symmetric about its own midplane (1/4 plane and 3/4 plane, respectively). Such a layup omits the bend/twist couplings and produces a quasi-isotropic behavior [17]. Therefore, only the bending stiffness of the plates can be varied by changing the laminate thickness t, which is done by adding $[0, 90]_s$ layers in the midplane. As a consequence of this addition, the axial stiffness quasi-isotropic behavior is lost, but the quasi-isotropy of the bending stiffness is conserved. Wings featuring these plates are named A to C, in increasing stiffness order. The different thicknesses are selected by taking into account the deflections obtained from the numerical model to avoid the FWT to move out of the wind-tunnel test section.

On the other hand, symmetric-only laminates that include the bend/twist coupling are used in the tailored wings. The stacking sequence of these laminates is optimized to maximize the bend/twist

---

¶See "BMS-A10H," Blue Bird Model, 2021. https://www.blue-bird-model.com/products_detail/73.htm [retrieved 28 July 2021].

***See "Arduino Boards and Modules," Arduino, 2021. https://store.arduino.cc/collections/boards [retrieved 25 May 2021].
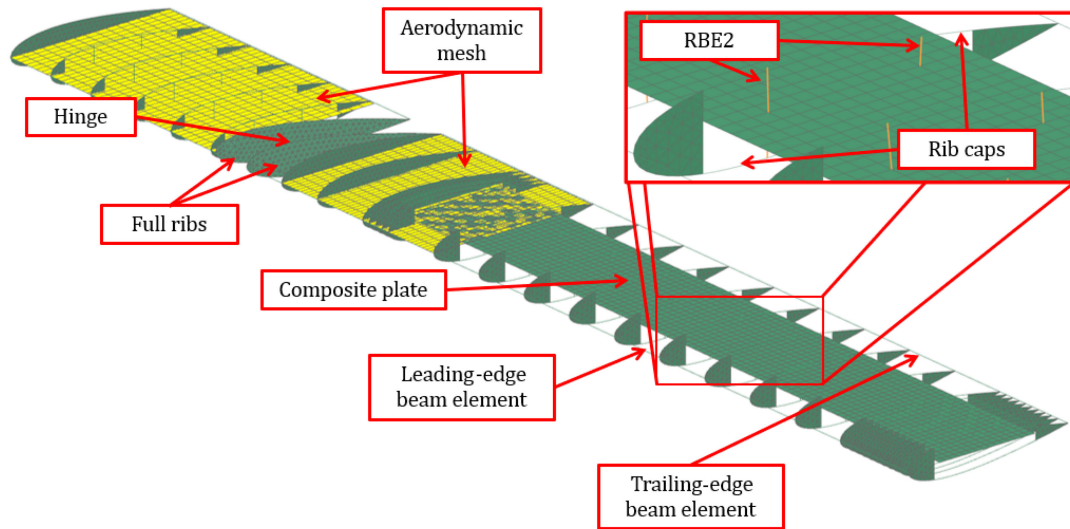
Fig. 3   FE model of the wing with a detail of the rib and the glue connection to the plate. Structural elements represented in green and aerodynamic mesh represented in yellow.

a) Simcenter 3D FEM representation of the hinge   b) Sketch of the connections used to model the hinge
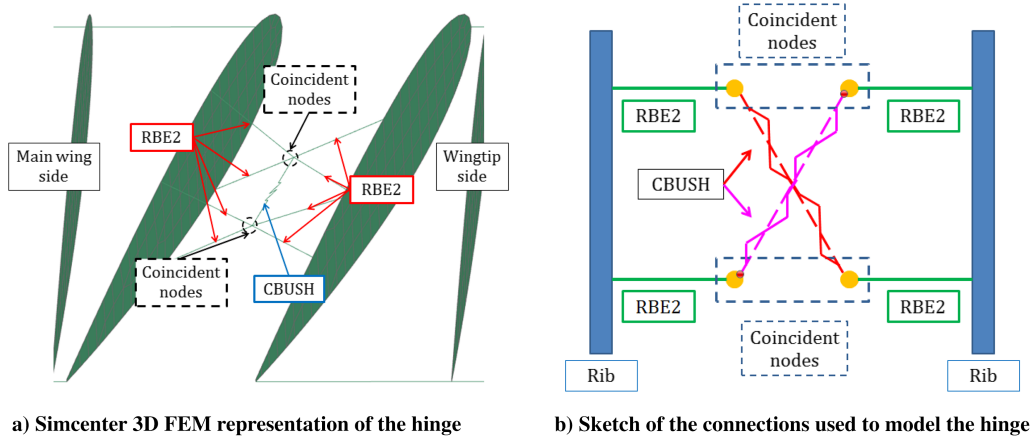
Fig. 4   Details of the FEM used for the hinge.

term of the compliance matrix d_{16}, while keeping the bending compliance term d_{11} within $\pm 2\%$ of the reference plate value of wing B. Consequently, the wings featuring wash-in and washout composite tailoring are designated B_{WI} and B_{WO}, respectively.

According to the classical laminate plate theory (CLPT) [17] and using the reference system introduced in Fig. 1, for a pure bending load, M_x, a nonzero d_{16} term would produce a rotation K_s around the longitudinal axis of the plate x. Thus, maximizing or minimizing this term maximizes the wash-in or washout response, respectively.

The optimization process uses the ply angles as design variables and computes the compliance matrix of the laminate by using CLPT. The total number of plies in the laminate $2n$ is the same as the reference laminate used in wing B, and the stacking sequence is defined as symmetric, which halves the number of design variables to n plies, and the b matrix becomes zero, eliminating the in-plane/out-of-plane couplings. The main constraint of the optimization problem is to achieve bending compliance terms similar to the reference value from wing B, and hence the relative difference between the bending compliance terms is constrained to $\varepsilon_{d_{11}}$, equivalent to a 2% difference. In addition, the extension/shear coupling terms of the a matrix a_{16} and a_{26} are constrained to small values $\varepsilon_{a_{16}}$ and $\varepsilon_{a_{26}}$, respectively, to maintain similarity with respect to the reference plate. Furthermore, the design space is reduced to ply angles from -90 to 90 deg in steps of 15 deg to simplify the manufacturing process and limit the possible outcome of the optimization.

Given the simplicity of the laminate model and the high number of design variables, the optimization problem is solved using the genetic

algorithm (GA) included in MATLAB®'s Global Optimization toolbox [18]. The GA depends on the initial conditions and randomization of each generation; therefore, the optimization problem is repeated 2000 times with randomized initial conditions to estimate the global optimum and create a set of possible laminates, from which the final design is selected by taking into account its sensitivity to variations of the ply angles to minimize the effect of manufacturing inaccuracies when the plates are produced for the experiment. Notice also that, thanks to the symmetry condition, rotating the plate 180 deg about the longitudinal axis of the wing produces the same bending properties but coupling properties change in sign. Thus, the optimization process can be carried out once for the wash-in design and then rotated about the symmetry plane to create the washout design. The optimization problem is presented in Eq. (1),

$$\underset{x}{\text{minimize }} d_{16}$$

$$\text{subject to } \left| \frac{d_{11}}{d_{11,\text{ref}}} - 1 \right| < \varepsilon_{d_{11}} = 0.02$$

$$|a_{16}| < \varepsilon_{a_{16}} = 10^{-9}$$

$$|a_{26}| < \varepsilon_{a_{26}} = 10^{-9} \qquad (1)$$

where $x = [\theta_1, \theta_2, \ldots \theta_n]$ and $\theta_i = [-75:15:90]$ for $i = 1, 2, \ldots, n$.

To conclude, the selected stacking sequences and the pertinent structural properties are presented in Table 2. Furthermore, Fig. 5 presents the engineering modulus of elasticity $\tilde{E}_{11}(\theta)$ and the bending

Table 2   Summary of selected wing core plates; stacking sequences are defined using the reference system in Fig. 1

Plate	Stacking sequence	d_{11}, $1/(\text{N} \cdot \text{mm})$	t, mm	Coupling	d_{16}, $1/(\text{N} \cdot \text{mm})$
A	$[0, 45, 90, -45]_s[[0, 90]_s]_s[0, -45, 90, 45]_s$	$1.82 \cdot 10^{-4}$	1.2	——	0
B	$[[0, 45, 90, -45]_2]_s[[0, -45, 90, +45]_2]_s$	$7.67 \cdot 10^{-5}$	1.6	——	0
C	$[[0, 45, 90, -45]_2]_s[[0, 90]_s]_s[0, -45, 90, +45]_2]_s$	$4.04 \cdot 10^{-5}$	2.0	——	0
B_{WI}	$[-30, -15, -45, -15_2, 75, \mp 30, 90, -75, 30, 15, -75, 45_2, 15]_s$	$7.64 \cdot 10^{-5}$	1.6	Wash-in	$6.19 \cdot 10^{-5}$
B_{WO}	$[30, 15, 45, 15_2, -75, \pm 30, 90, 75, -30, -15, 75, -45_2, -15]_s$	$7.64 \cdot 10^{-5}$	1.6	Washout	$-6.19 \cdot 10^{-5}$

modulus of elasticity $\tilde{D}_{11}(\theta)$ computed from the *abd* matrix as presented in Eq. (2) [19].

$$\tilde{E}_{11}(\theta) = \frac{1}{a_{11}(\theta)}; \quad \tilde{D}_{11}(\theta) = \frac{1}{d_{11}(\theta)}$$

$$a(\theta) = T^T a T; \quad d(\theta) = T^T d T \qquad (2)$$

where

$$T = \begin{pmatrix} \cos^2(\theta) & \sin^2(\theta) & 2\cos(\theta)\sin(\theta) \\ \sin^2(\theta) & \cos^2(\theta) & -2\cos(\theta)\sin(\theta) \\ -\cos(\theta)\sin(\theta) & \cos(\theta)\sin(\theta) & \cos^2(\theta) - \sin^2(\theta) \end{pmatrix} \qquad (3)$$

This comparison shows the variation in bending stiffness between plates A to C and the variation in directional properties between the tailored plates B_{WI} and B_{WO} and the reference plate B. The properties along the longitudinal axis of the plate, $\theta = 0$ deg, are also presented in Table 2.
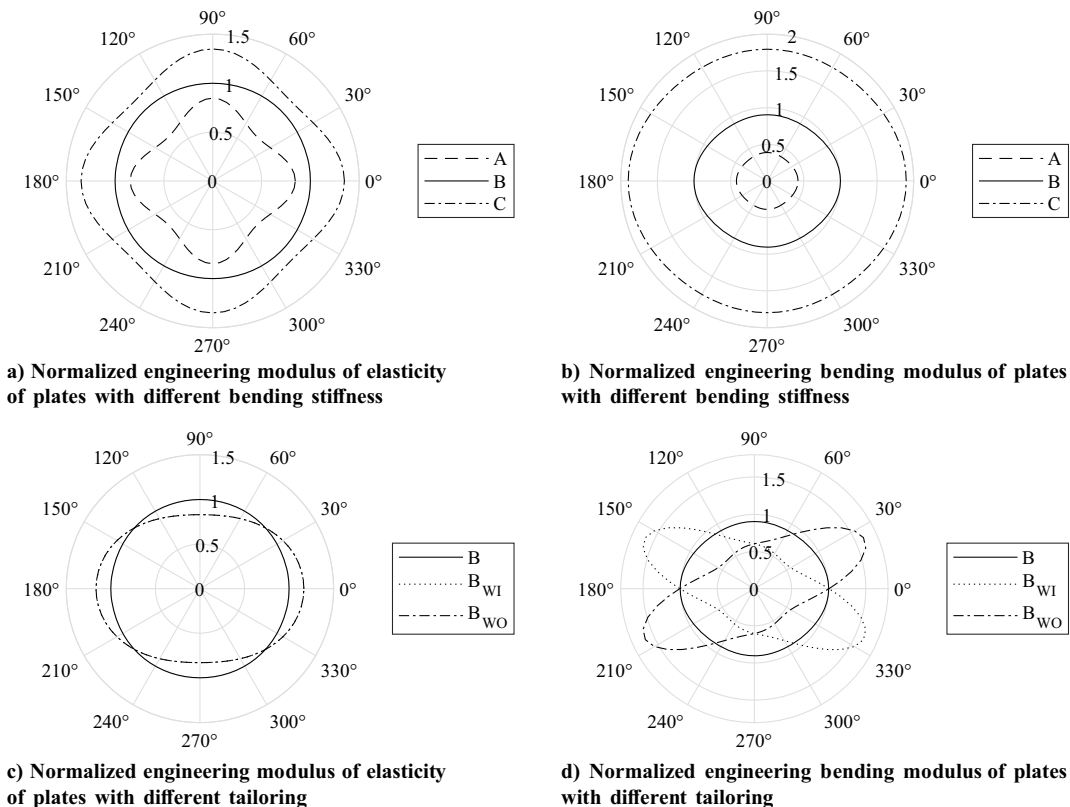
D. Numerical Simulations

First, the normal modes of the wing are computed using SOL 103, leading to the flutter analysis using SOL 145. The first three natural frequencies of each of the wings in both locked-hinge and free-hinge conditions are presented in Table 3. In addition, the corresponding

Table 3   Comparison between wings of natural frequencies of first modes of free-hinge and locked-hinge configurations (SOL 103/SOL 145)

Mode	A	B	C	B_{WI}	B_{WO}
Locked: 1st bending, Hz	2.91	3.20	3.60	3.28	3.27
Locked: 2nd bending, Hz	16.48	17.25	18.13	17.46	17.50
Locked: 1st torsion, Hz	30.55	34.30	39.98	34.13	34.35
Free: 1st flapping, Hz	1.23	1.24	1.25	1.24	1.24
Free: 2nd flapping, Hz	4.36	4.74	5.28	4.86	4.84
Free: 1st torsion, Hz	28.00	30.78	33.93	30.64	32.03

modal shapes are presented in Fig. 6, which shows that the free-hinge modes, referred to as flapping modes, show considerable wingtip deflection in addition to the wing deformation.

Subsequently, the results of the flutter analysis are summarized in Table 4. The bending stiffness of the wings increases the flutter speeds, as can be concluded from the results of wings A, B, and C. In addition, in the free-hinge condition, the flutter speed experiences a significant drop with respect to the locked-hinge condition. For a better understanding of this phenomenon, the sensitivity of the flutter speed with respect to the changes in the hinge stiffness is investigated by gradually increasing the hinge stiffness from 1 $(N \cdot mm)/\text{rad}$ to the stiffness in the locked-hinge condition, as shown in Fig. 7. A clear jump in flutter speed occurs between hinge stiffness of 50 and

a) Normalized engineering modulus of elasticity of plates with different bending stiffness

b) Normalized engineering bending modulus of plates with different bending stiffness

c) Normalized engineering modulus of elasticity of plates with different tailoring

d) Normalized engineering bending modulus of plates with different tailoring

Fig. 5   Comparison of $\tilde{E}_{11}(\theta)$ (left) and $\tilde{D}_{11}(\theta)$ (right). Parameters normalized with maximum value of reference plate, B.

a) Locked hinge, 1st bending mode

b) Free hinge, 1st flapping mode

c) Locked hinge, 2nd bending mode

d) Free hinge, 2nd flapping mode

e) Locked hinge, 1st torsion mode
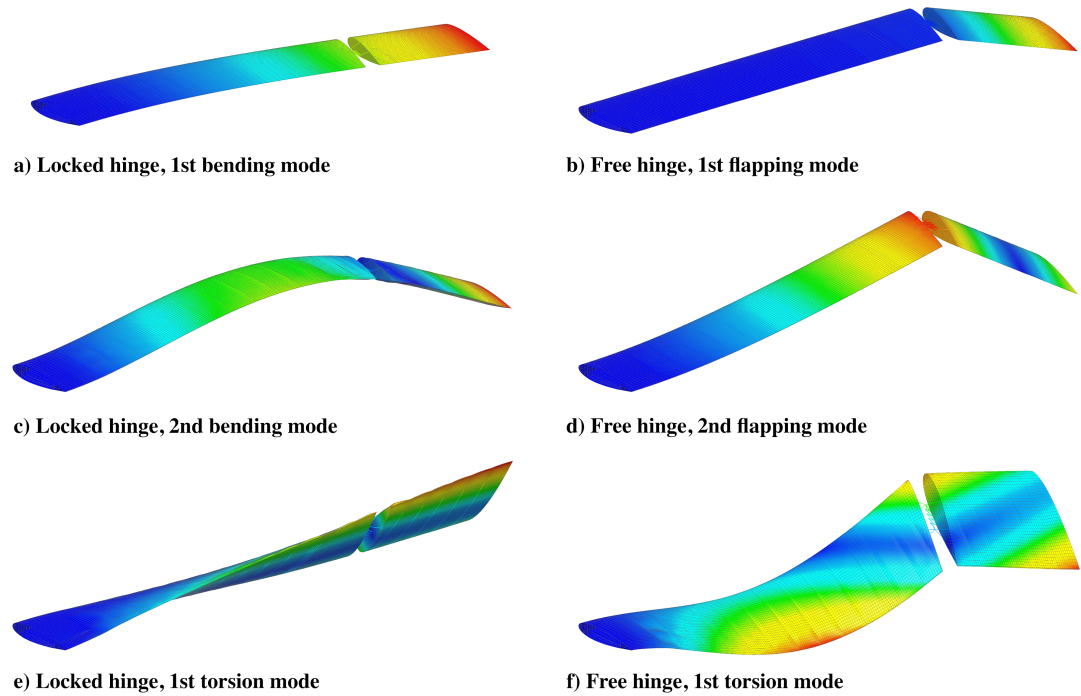
f) Free hinge, 1st torsion mode

Fig. 6   Natural modes from simulation (SOL 103/SOL 145).

Table 4   Instability speed comparison between wings in free-hinge and locked-hinge conditions (SOL 145)

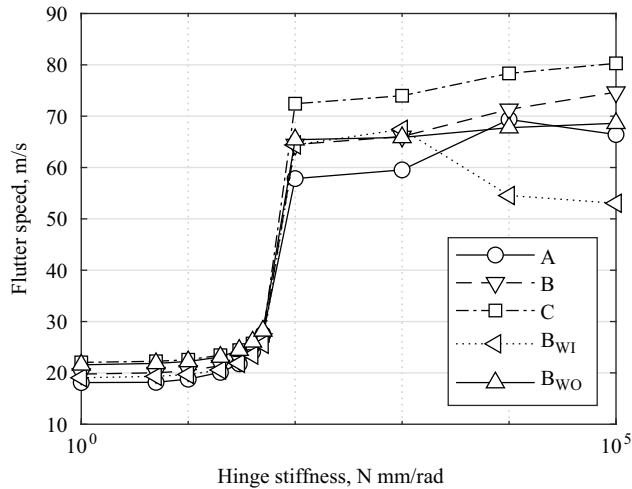| Wing	A	B	C	B_{WI}	B_{WO}
Free hinge, m/s	18.0	19.7	22.0	19.0	21.5
Locked hinge, m/s	66.0	74.7	80.3	53.0	68.6

Fig. 7   Sensitivity analysis of flutter speed to hinge stiffness for the different wings.

100 (N · mm)/rad. To explain the reason for this jump, Fig. 8 presents the damping and frequency diagrams for the cases close to the sudden variation. For lower stiffness, it can be seen that the positive damping coefficient appears in the second flapping mode driven by an interaction with the first flapping mode. However, at higher speeds, the second flapping mode becomes stable again, while the first flapping mode starts to interact with the first torsion mode, which becomes unstable. On the other hand, for the increased stiffness, the flapping modes become bending modes, and the first flutter mechanism disappears, which leads to flutter driven by a first-torsion/second-bending

interaction, similar to the second flutter mechanism seen in the free-hinge condition. Thus, the speed drop between conditions is caused by a change in the flutter mechanism that drives the instability.

Finally, the flutter analysis also shows interesting behavior with respect to the wing tailoring and free-hinge and locked-hinge conditions. Considering the reference studies on aeroelastic tailoring presented by Weisshaar [13], it is expected that the wash-in tailoring delays flutter and promotes divergence while the washout tailoring has the opposite effect. To explain the behavior in the locked-hinge condition, which would correspond to a conventional wing, Fig. 9 presents a comparison of the damping and frequency flutter plots of wings B, B_{WI} and B_{WO}. For wing B_{WI}, there is a sudden drop in damping coefficient and frequency of the first bending mode, representative of a divergence instability. In contrast, the limiting aeroelastic instability for wings B and B_{WO} is flutter. Nevertheless, when comparing the flutter speed of the tailored wings, the flutter speed of the B_{WI} is higher than the flutter speed of the B_{WO}. These observations are in agreement with the expectations presented by Weisshaar.

On the other hand, in the free-hinge condition, the limiting instability is flutter in all the wings. However, in this case, the flutter speed of the B_{WI} is lower than that of the B_{WO}, which is contrary to the expectations [13]. This finding could be explained by the change in the flutter mechanism seen in the hinge stiffness sensitivity analysis; hence, the design rules applied for conventional aircraft wings might not be applicable for the FWT.

To conclude the flutter analysis, the sensitivity of the instabilities to the hinge stiffness and the change in the flutter mechanism show the complexity of the structural response of the hinge, and the drop in flutter speeds presents a possible limitation of the FWT. Keeping this in mind, the experiment is designed at an airspeed of 15 m/s to avoid unexpected instabilities.

Next, static aeroelastic simulations using SOL 144 are used to estimate the steady-state loads and deflections of the wing. These simulations include gravity and study the wing at $\alpha = 0$ deg and $\alpha = 8$ deg. On the one hand, because the airfoil used is symmetric and given the assumptions of the aerodynamic model, the first condition is equivalent to a static simulation in which the model is only loaded by gravity. On the other hand, the $\alpha = 8$ deg condition introduces an aerodynamic load to compare it with the magnitude of the weight and study, which force is dominant. To make it as similar as possible to real flight conditions, it is desired to have a system whose response is dominated by the aerodynamic force, so

a) $K_\beta = 50$ (N·mm)/rad   **b) $K_\beta = 100$ (N·mm)/rad**
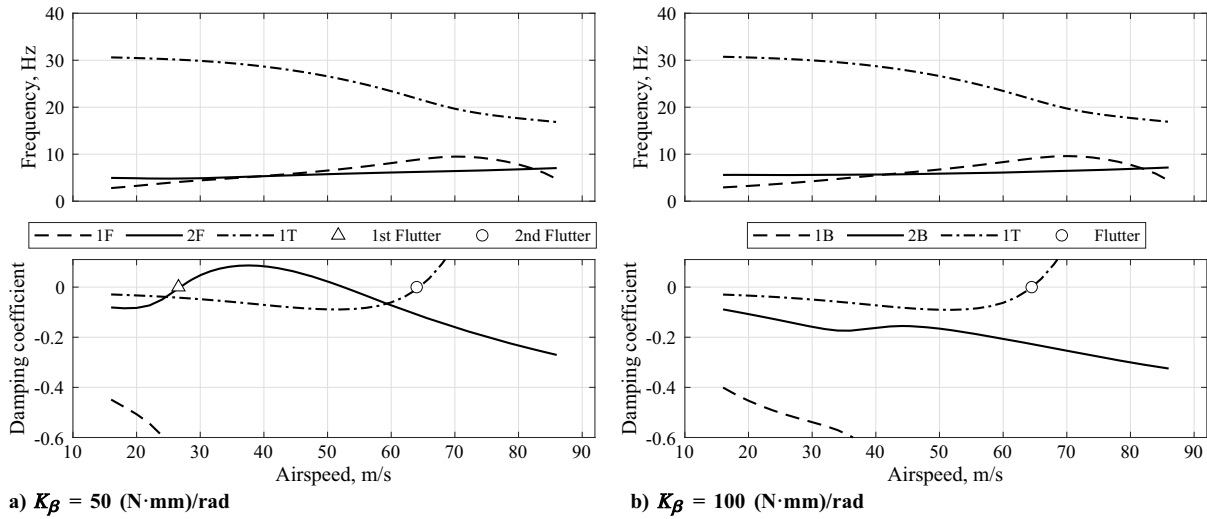
Fig. 8   Comparison of $V - g$ and $V - f$ flutter plots of wing B at different hinge stiffnesses K_β. Only flapping (F), bending (B), and torsion (T) modes represented.

a) Wing B_{WI}   **b) Wing B**

c) Wing B_{WO}
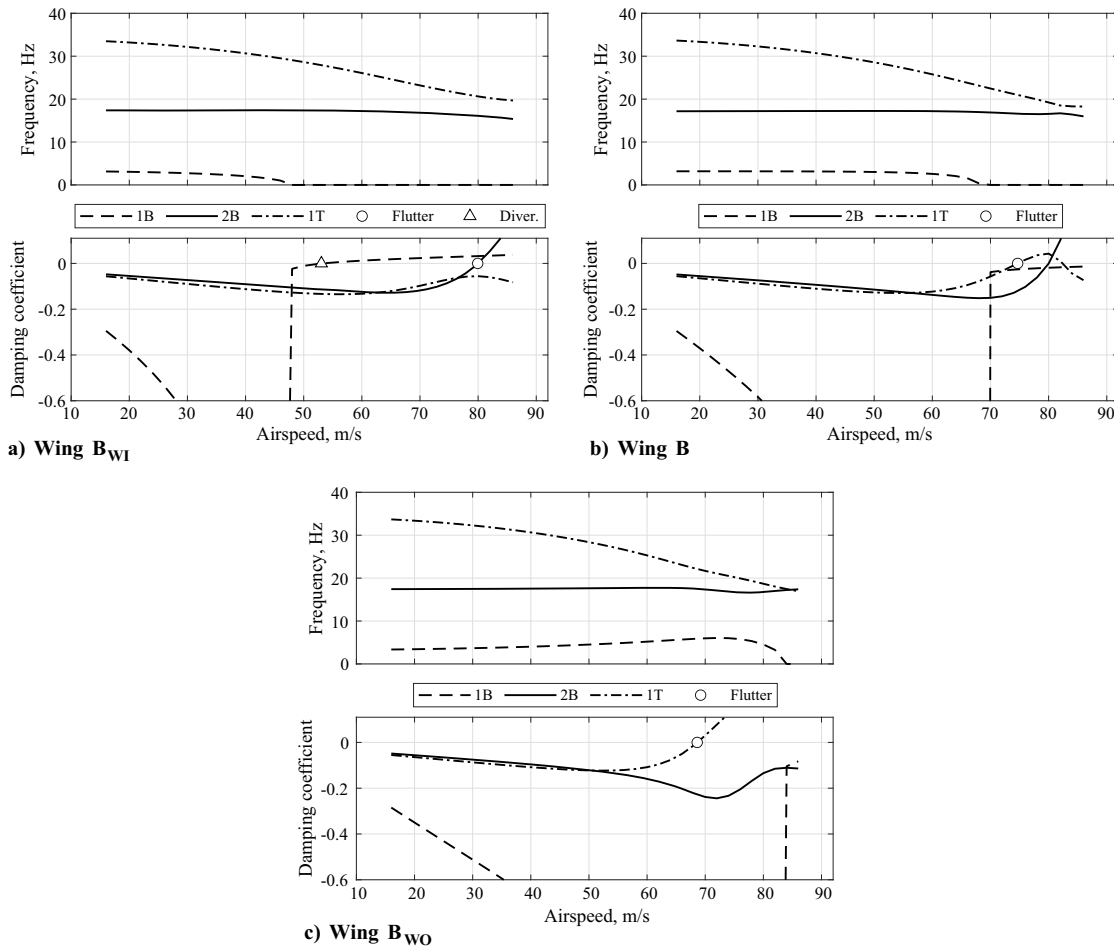
Fig. 9   Comparison of $V - g$ and $V - f$ flutter plots between wings B, B_{WI} and B_{WO}, in locked-hinge condition. Only bending (B) and torsion (T) modes represented.

the 3D printed part is optimized to reduce its weight using these simulations as reference.

Finally, the gust response is studied with SOL 146. As explained by Cheung et al. [5], it cannot be used to solve gusts hitting the wing at a given static condition, in other words, $\alpha \neq 0$ deg, so the problem is solved as a superposition of the static condition and the gust. First, the mesh is predeformed according to the results of the static analysis, and,

afterward, the gust is simulated. The final result is then the sum of both. Notice that, given the linearity of the model, the validity of the results is limited to low fold angles β. For this reason, the locked-hinge condition is considered as an indicator of the maximum load and deflections, but the free-hinge condition is only considered qualitatively to understand its effects. The hinge release based on a load threshold cannot be simulated with the available tools; hence, it is not considered.
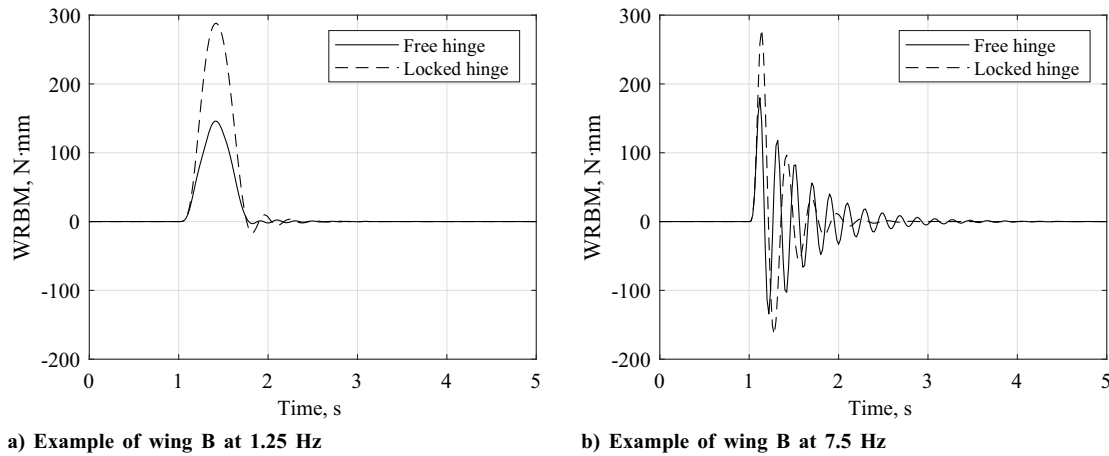
a) **Example of wing B at 1.25 Hz**   b) **Example of wing B at 7.5 Hz**

Fig. 10   Results of gust simulations (SOL 146). Comparison between locked-hinge and free-hinge conditions for different gust frequencies.

a) **Locked hinge**   b) **Free hinge**
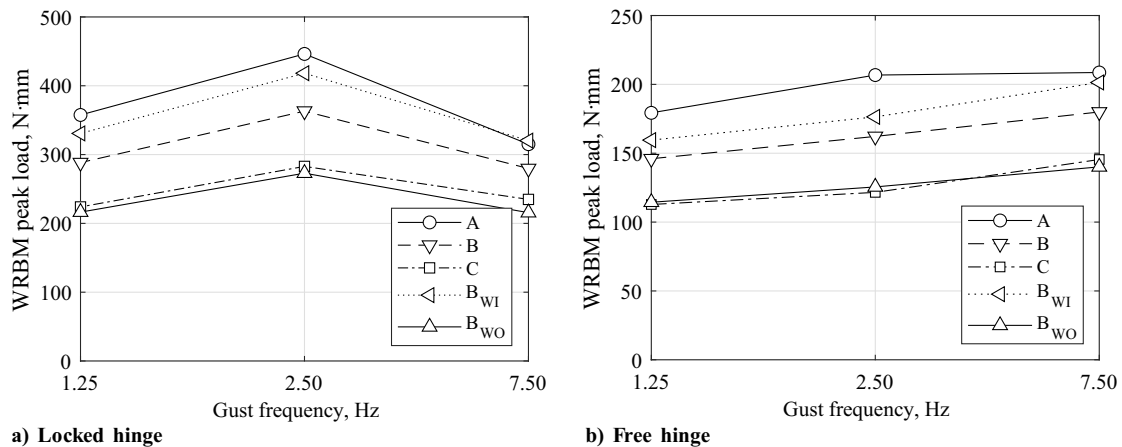
Fig. 11   Peak WRBM load comparison between plates for different gust frequencies (SOL 146).

These results are used to ensure the wing will remain in the wind-tunnel test section during the experiment and that the different designs offer a noticeable difference in their response. Figure 10 shows an example of a comparison between the locked-hinge and free-hinge conditions for two different gusts, and Fig. 11 shows a comparison of peak loads between wings at different gust frequencies.

From the individual gust responses, it is possible to see that the peak loads are of similar amplitude regardless of the gust frequency; however, the overall time response depends significantly on the gust frequency. On the one hand, for the low-frequency gust of 1.25 Hz, the loads smoothly follow the gust and present a small oscillation after the gust when the hinge is locked. On the other hand, for the high-frequency gust of 7.5 Hz, there is a clear difference between the free-hinge and the locked-hinge conditions. While the oscillations disappear after a second for the locked-hinge condition, the oscillations persist for twice the time in the free-hinge condition. This behavior is similar for all the wings, and hence only these examples are presented.

Finally, in the peak load comparison, there is a clear difference between the magnitudes each wing can achieve. The peak loads decrease with the bending stiffness of the wings; hence, wing A presents higher peak loads than wing B, and wing B presents higher peak loads than wing C. Furthermore, the tailoring also has a prominent effect: wing B_{WO} presents the lowest peak loads, even lower than wing C, while B_{WI} shows higher peak loads than the reference wing B, comparable to those from wing A.

III.   Wind-Tunnel Experiments

The wind-tunnel experiments, including the test setup, the sensors used, and the data acquisition procedure, are described in this section.

Subsequently, the complete measurement procedure and data post-processing are described in more detail.

A.   Test Setup

The experiments are conducted in the W-Tunnel at the Delft University of Technology, which is an open jet wind tunnel with a square test section of 0.40×0.40 m^2. The tests are performed at a freestream velocity of 10 m/s, which has to be reduced with respect to the design freestream velocity due to the occurrence of flutter, as further addressed in Sec. IV. A gust generator with a contraction to a 0.40×0.35 m^2 test section is mounted at the outlet of the tunnel nozzle to create the gust perturbations. An overview of the gust generator and the wing model is presented in Fig. 12.

Figure 13 shows the sensors mounted on the wing. Two Kyowa KFGS-10-120-D17-16[†††] triaxial 0/45/90 deg strain gauge rosettes are used on the top and bottom faces of the plates to measure the deformation at the root of the wing, which is related to the WRBM. The central strain gauge, 45 deg, is positioned in the spanwise direction, leaving the 0 and 90 deg strain gauges at ± 45 deg from the spanwise direction of the wing. Each of the top strain gauges is connected to the corresponding parallel strain gauge from the bottom rosette in half-bridge configuration. Second, two PCB 352A24 uni-axial accelerometers[‡‡‡] are used to characterize the main wingtip displacement. Finally, the fold angle of the wingtip is measured with a

[†††]See "KFGS Series, General-purpose Foil Strain Gages," KYOWA, 2021, https://www.kyowa-ei.com/eng/product/category/strain_gages/kfgs/index.html [retrieved 28 July 2021].

[‡‡‡]See "PCB 352A24 Uniaxial Accelerometer," PCB Piezotronics, 2021, https://www.pcb.com/products?model=352A24 [retrieved 28 July 2021].
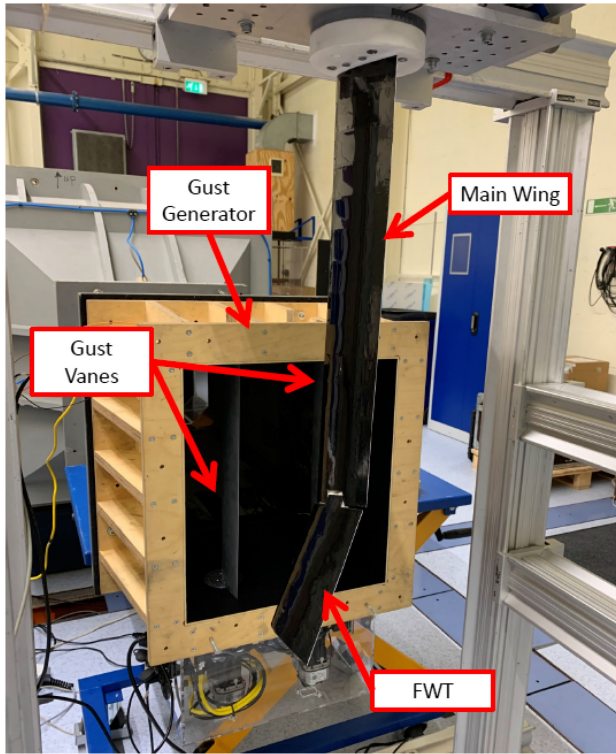
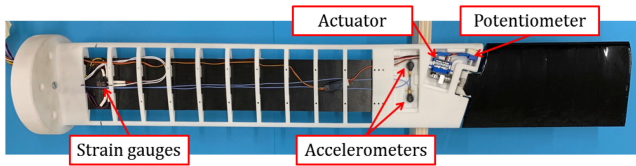**Fig. 12   Overview of the gust generator and test object.**

Fig. 13   Distribution of sensors along the wing.

Bourns 3310C-125-203L potentiometer[§§§] connected to the shaft of the FWT.

The data acquisition is implemented by the system presented in Fig. 14. The gust generator creates a sequence of 1-cosine gusts with a fixed time interval. At the start of each gust, a trigger signal is generated and sent to both an Arduino UNO (see footnote ***) and a SCADAS Mobile[¶¶¶] The Arduino UNO is used to control the hinge release: when the trigger is received, the microcontroller waits for a specified time, which is tuned to correspond to a specific load threshold, and then releases the mechanism. After a few seconds, the hinge is taken back to the locked position. The SCADAS is in charge of the data acquisition; it reads all the sensors as well as the trigger signal from the gust generator and a control signal generated by the Arduino in order to keep track of the actuator motion and the measurements in a synchronized manner. Finally, the SCADAS information is sent to a National Instruments cRIO-9744[****] to process and save the measurements in the main computer.

B.   Experimental Procedure

1.   Strain Gauge Calibration

The strain gauge bridge requires a calibration to allow for the determination of the loads from the bridge output. The linear transformation

[§§§]See "Bourns 3310 series," Bourns, 2021. https://www.bourns.com/products/potentiometers/industrial-panel-controls/product/3310 [retrieved 28 July 2021].

[¶¶¶]See Simcenter SCADAS Mobile and SCADAS Recorder, Siemens - Community support, 2021. https://community.sw.siemens.com/s/article/simcenter-scadas-mobile-and-scadas-recorder [retrieved 28 July 2021].

[****]See cRIO-9074, National Instruments - Support, 2021. https://www.ni.com/nl-nl/support/model.crio-9074.html [retrieved 28 July 2021].

$\bar{c}$ is a matrix that relates the bending loads M_X and torque loads M_S to the strain gauge bridge signals G as presented in Eq. (4):

$$\begin{pmatrix} G_{+45} \\ G_0 \\ G_{-45} \end{pmatrix} = \bar{c} \begin{pmatrix} M_X \\ M_S \end{pmatrix} = \begin{pmatrix} c_{1,1} & c_{1,2} \\ c_{2,1} & c_{2,2} \\ c_{3,1} & c_{3,2} \end{pmatrix} \begin{pmatrix} M_X \\ M_S \end{pmatrix} \qquad (4)$$

By applying pure bending and torque loads separately [20,21], it is possible to obtain the calibration constants $c_{i,j}$ using the least-squares (LS) solution according to Eq. (5), where $\boldsymbol{M_j}$ and $\boldsymbol{G_i}$ are vectors of known loads and the signal of the strain gauge in i direction, respectively,

$$\boldsymbol{G_i} = c_{i,j} \cdot \boldsymbol{M_j} \rightarrow c_{i,j} = \left(\boldsymbol{M_j^T M_j} \right)^{-1} \boldsymbol{M_j^T G_i} \qquad (5)$$

Once the calibration constants are known, the inverse transformation $\bar{C}$ can be computed using the pseudoinverse concept already used in the LS solution:

$$\boldsymbol{G} = \bar{c} \boldsymbol{M} \rightarrow \left(\bar{c}^T \bar{c} \right)^{-1} \bar{c}^T \boldsymbol{G} = \boldsymbol{M} \rightarrow \boldsymbol{M} = \bar{C} \boldsymbol{G} \qquad (6)$$

Finally, this calibration is validated by applying a combination of bending and torsion loads and comparing them to the loads obtained after transforming the strain gauge signals with the calibration matrix. As shown in Table 5, the maximum error for the bending moment is below 10%. However, the average error in the torque measurement is 40% and is very inconsistent between wings. These differences are attributed to the cross-measurement of the bending and torsional loads by the ±45 deg strain gauges, which are affected by both loads. Because the bending loads are higher than the torsional loads, the measurements of these strain gauges are dominated by bending, which affects the calibration matrix. Given this limitation, the torsional load is not considered in the results.

2.   Test Procedure

The experiment is carried out for each of the wings presented in Table 2. The investigation starts with characterizing the static behavior of the wings by changing the angle of attack α between −6 and 14 deg. These measurements are collected in polar curves of the bending moment coefficient C_B, defined by Eq. (7), and the fold angle β,

$$C_B = \frac{M_X}{(1/2)\rho SBU^2} \qquad (7)$$

Next, the time response of the wings to a 1-cosine gust excitation is recorded for different angles of attack, gust frequencies, and release thresholds. The variation in the angle of attack separates a purely dynamic load ($\alpha = 0$ deg) from a more representative combination of dynamic and static load introduced by a nonzero angle of attack ($\alpha = 5$ deg). The gust frequencies selected for the experiment are spread below, above, and close to the natural frequencies in free-hinge and locked-hinge conditions to cover a broad dynamic range. The first natural frequency in the locked-hinge configuration is referred to as first bending, while the first one in the free-hinge condition is referred to as first flapping. These natural frequencies are found with a modal impact test, which is performed in situ when the wing is mounted in the wind tunnel.

Finally, the threshold variations include the free-hinge and locked-hinge conditions as a reference and different release conditions during the gust: 1) released with the gust generator trigger signal before the gust hits the wing; 2) when the gust hits the wing, in other words, the load starts increasing; 3) it is released when the load achieves 50% of its peak load; and 4) at the peak load. These release conditions are referred to as prereleased, 0, 50, and 100% release, respectively. An overview of the test cases is presented in Table 6. For each specific dynamic testing condition, the experiment is repeated
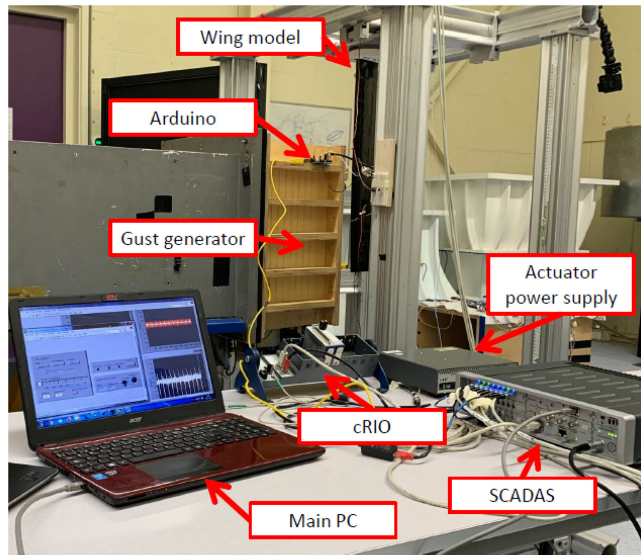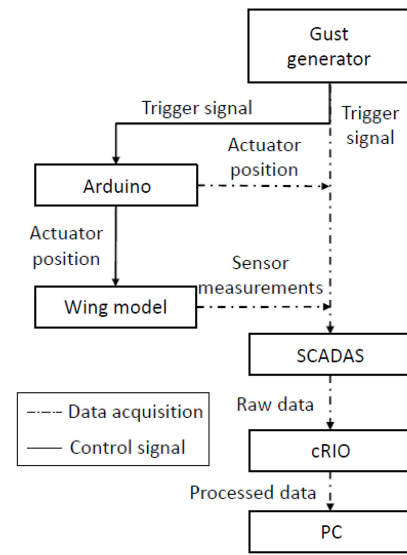
a) Wind-tunnel setup   b) Data flow schematic

Fig. 14   Wind-tunnel setup and data acquisition system overview.

Table 5   Comparison of maximum relative error between the calibrated measured load and the applied load

Wing	A	B	C	B_{WI}	B_{WO}
Bending, %	5.5	−7.7	6.8	−6.5	−3.6
Torque, %	81.2	14.4	−23.8	36.7	35.9

Table 6   Overview of test cases

Parameter	Static load	1-cosine gust
Plate	A, B, C, B_{WI}, B_{WO}	— —
Hinge condition	Free, Locked, Pre-released, 0%, 50%, 100%	— —
α, deg	[−6, 14]	0, 5
Gust amplitude, deg	— —	2.5
Gust frequency, Hz	— —	0.5, 5, 8, 1st bending, 1st flapping

ten times to allow for statistical evaluation of the measured aeroelastic responses.

3.   Measurement Postprocessing

The assessment of the results is carried out using two main parameters: peak loads and root mean square (RMS). Figure 15 shows an example of the variation of the bending moment coefficient

Fig. 15   Quantities used for processing the data.

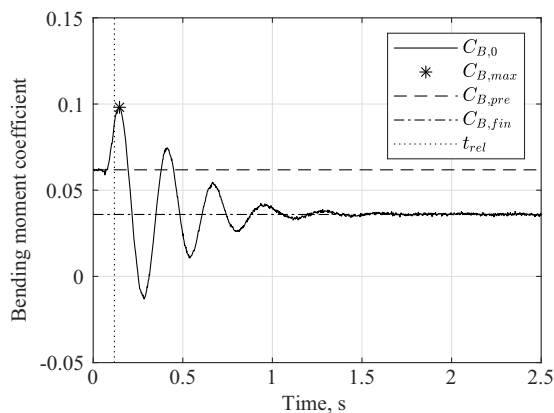over time at $\alpha = 5$ deg. The peak load ΔC_B is defined as the difference between the maximum load $C_{B,\max}$ and the mean prerelease steady-state load $C_{B,\mathrm{pre}}$, in other words, the static load before the gust hits the wing.

The RMS is used as an indicator of the persistence of the oscillations in the load signals. After the gust encounter, the dynamic load settles on the static load corresponding to the locked-hinge or free-hinge condition. Therefore, the oscillations that persist for a longer time result in a higher RMS value. Because there are two steady states corresponding to the locked-hinge and free-hinge conditions, as seen in Fig. 15, the RMS is calculated using $\tilde{C}_B(t)$, as defined in Eq. (8):

$$
\tilde{C}_B(t) = \begin{cases} C_{B,0}(t) - C_{B,\mathrm{pre}} & \text{for } 0 < t < t_{\mathrm{rel}} \\ C_{B,0}(t) - C_{B,\mathrm{fin}} & \text{for } t > t_{\mathrm{rel}} \end{cases} \tag{8}
$$

IV.   Results

The experimental results are presented in this section and, where possible, compared with the numerical results. In the initial phase of the wind-tunnel campaign, it was discovered that the actual flutter speed was considerably lower than expected. As a result, the free-stream velocity of the wind tunnel had to be reduced from 15 to 10 m/s to operate in safe, flutter-free conditions across all the wings. Consequently, it was decided to measure the wings in a vertical orientation to avoid their response being dominated by weight rather than aeroelastic forces.

A.   Test Conditions: Flutter

After the first design space exploration, a stability study is carried out for each wing. The airspeed is increased in steps of 1 m/s, corrected to account for the gust generator contraction, and the wing is excited to observe its response. The wing is considered unstable when the transient response fails to die out. First, the locked-hinge condition was tested. No flutter speed was observed for the free-stream velocity up to 25 m/s, which is consistent with the numerical predictions foreseeing the flutter onset only at 66 m/s. In the next step, the flutter was assessed in the free-hinge condition. The results of the comparison between wings are presented in Fig. 16, with the numerical results and the measured flutter speeds at $\alpha = 0$ deg presented in Table 7.

Figure 16 shows the dependency of flutter onset velocity on the angle of attack, α. One can observe that, with increasing α, the flutter onset velocity is reduced, which is attributed to an effect already observed in highly flexible wings [22,23]. The large deflections affect the frequency separation between the modes comprising the
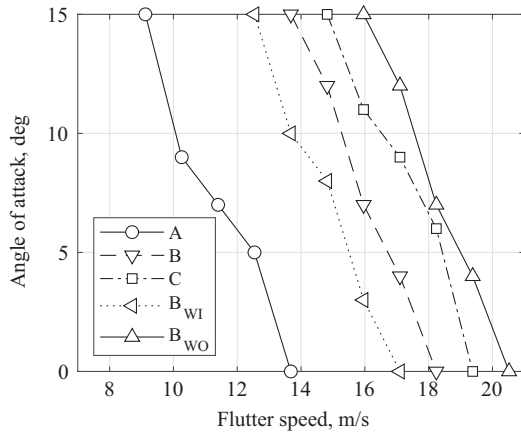
Fig. 16 Comparison of flutter speeds at different angles of attack for each wing.

flutter mechanism, which leads to a reduction of the flutter onset velocity when increasing α (i.e., the out-of-plane deflection).

In addition, when comparing the results at $\alpha = 0$ deg, it can be seen how the trends observed in the experimental results are the same observed in the simulations but at lower speeds. The increase in the flutter speed across wings A, B, and C follows the numerical predictions, with wing A exhibiting the lowest flutter speed and wing C exhibiting the highest flutter speed. Considering the tailored wings, the flutter speed of wing B_{WI} is lower than that of wing B, while the flutter speed of wing B_{WO} is higher, which is in agreement with the observations presented in Sec. II.B. In this regard, the experiments confirm that the FWT in a free-hinge condition can considerably alter the aeroelastic stability behavior of tailored composite wings.

B. Natural Modes: Modal Impact Test

Table 8 compares the numerical and experimental results for the first natural frequencies of the tested wings in both locked and free-hinge conditions. It can be seen that the relative difference in the first bending mode is below 10%, while the first and second flapping modes present differences of −6 and 20%, respectively.

Notice also that the first flapping frequency is the same for all the wings and is nonzero, contrary to previous studies [7]. On the one hand, investigating the representation of the mode in the simulation, it can be seen that this mode is dominated by the wingtip motion, as shown in Fig. 6b, which explains why the frequency is independent of the structural properties. On the other hand, the nonzero frequency can be attributed to the vertical setup, which makes the wingtip behave like a pendulum. Furthermore, one can approximate this effect as an equivalent stiffness in the hinge, which was evaluated

to be 40 $(N \cdot mm)/rad$. As shown in Fig. 7, this stiffness is below the sudden jump in the flutter onset velocity; hence, it is considered that the aeroelastic behavior of the folding wingtip is not significantly affected by the vertical installation and associated gravity effects.

Finally, the first bending and first flapping frequencies are used as one of the gust excitation frequencies during the gust experiments to study the effect on the GLA performance of exciting the wings at their natural frequencies. However, the gust generator can only produce gusts of frequencies from 0.5 to 10 Hz in steps of 0.5 Hz; therefore, the excitation frequencies are rounded to the closest possible frequencies considering the results from the impact test. As a result, the first flapping frequency used in the experiment is 1.5 Hz for all the wings, and the first bending frequency is 3.0 Hz for all but wing C, which is tested at 3.5 Hz.

C. Static Load: Bending Polar

The bending moment coefficient polar is the first step to understanding the impact of the design variations on the exerted aerodynamic loads. Figure 17 shows the example of the bending moment coefficient and fold angle polars for wing B, which shows a behavior similar to the other wings. The load alleviation due to the released FWT can be clearly observed by the reduced slope of the bending moment coefficient line, which is in agreement with the observations presented by Cheung et al. [5]. Notice also that, for high angles of attack in the locked-hinge condition, the slope of the bending moment starts decreasing, while the measurement uncertainty starts increasing, which could be related to boundary-layer separation. On the other hand, similar behavior is not observed for the free-hinge condition. Furthermore, the fold angle polar shows how the FWT rotates to keep the load equilibrium when the hinge is released. In addition, for the example of wing B when the hinge is locked, the measured angle is not zero but varies in the range of ±1 deg. This could be caused by the compliance of the hinge locking mechanism, allowing some displacement of the FWT.

Table 9 presents a summary of the polar slopes of all the tested wings. On the one hand, wings A, B, and C present the same slope in the locked-hinge condition, which shows that the results are not significantly affected by the bending stiffness. On the other hand, due to the added bend/twist coupling caused by the washout tailoring of wing B_{WO}, the slope decreases. This behavior is reversed for B_{WI}, although the effect on the slope with respect to the reference wing, B, is not as clear as for B_{WO}. The asymmetry in the response between the tailored wings could be caused by imperfections in manufacturing, such as the alignment of the plate within the wing or the inconsistent shrinking of the skin foil.

Finally, when the hinge is released, wings A, B, and C present different slopes but do not follow a trend that could be related to the differences in bending stiffness. In addition, the slopes presented by the tailored wings are almost the same and lower than the reference slope of wing B, contrary to the expected results seen in the locked condition.

Table 7 Comparison between experimental and simulated flutter speeds for the free-hinge condition

Wing	A	B	C	B_{WI}	B_{WO}
Simulation, m/s	18.4	20.0	22.7	19.7	21.5
Experiment, m/s	13.7 (−25.4%)	18.2 (−9.1%)	19.4 (−14.7%)	17.1 (−13.1%)	20.5 (−4.7%)

Table 8 Comparison of natural frequencies obtained from modal impact test and simulation

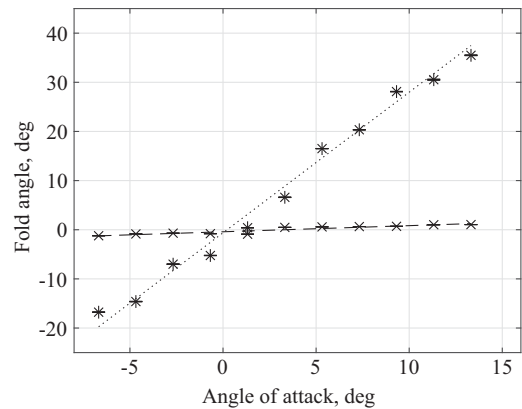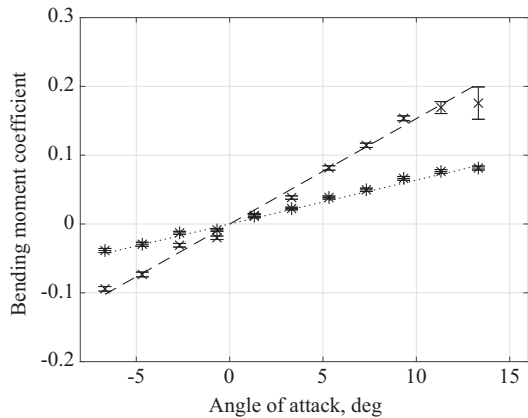| Wing	A		B		C		B_{WI}		B_{WO}	
Source	Experimental	Simulation	Experimental	Simulation	Experimental	Simulation	Experimental	Simulation	Experimental	Simulation
1st flapping, Hz	1.33	1.24 (−6.7%)	1.33	1.25 (−6.0%)	1.33	1.26 (−5.2%)	1.33	1.25 (−6.0%)	1.33	1.25 (−6.0%)
1st bending, Hz	2.76	3.05 (+10.5%)	3.03	3.33 (+9.9%)	3.42	3.70 (+8.2%)	3.23	3.46 (+7.1%)	3.23	3.31 (+1.9%)
2nd flapping, Hz	3.49	4.43 (+26.9%)	3.90	4.78 (+22.6%)	4.40	5.47 (+24.3%)	4.09	4.95 (+21.0%)	4.10	4.84 (+18.0%)

Fig. 17   Plate B interpolated C_B and β polars.

Table 9   Comparison of the slopes of the C_B polars of the different wings; slopes presented in counts ($C_B = 0.0001 = 1$ count)

Wing	Locked $C_{B,\alpha}$, 1/deg	Free $C_{B,\alpha}$, 1/deg
A	153	68
B	153	64
C	153	65
B_{WI}	156	56
B_{WO}	133	57

D.   Dynamic Load: 1-Cosine Gusts

The last part of the experiment studies the dynamic response of the wing when hit by 1-cosine gusts to assess the GLA performance of the FWT. Before addressing the results, the response of the system is characterized by studying the time delays introduced during the actuation process.

1.   System Characterization

When studying the time response of the different wings, it is found that the release time of the wingtip hinge, corresponding to a specific load threshold, has a great impact on the FWT performance. For this reason, it is necessary to characterize the hinge release process in terms of time delays before addressing the GLA performance. There are two sources of possible time delay.

The first source of time delay originates from the Arduino requiring time to process the input and release the hinge. As seen in Sec. III.A, the microprocessor adds a delay to release the hinge at the desired load threshold. To know how precise this release is, the desired delay is compared to the elapsed time between reading the trigger signal from the gust generator and reading the control signal obtained from the Arduino, which controls the position of the actuator. This delay is analyzed across all the test cases and amounts to an average delay of 2 ms with a standard deviation of 1.3 ms.

The second source of the time delay originates from the time it takes between issuing the hinge release command and the wingtip to start moving. To study this delay, the release time is compared to the potentiometer position. The wingtip is considered to start reacting when the potentiometer position changes by more than 1 deg. A representation of this time delay is presented in Fig. 18, which shows that the potentiometer signal does not change immediately after sending the release command to the actuator. It is found that this delay is 50 ms on average with a standard deviation of 7 ms.

The importance of these delays depends on the gust frequency as quantified in Table 10 by converting the time delays into relative delays with respect to the gust period. The 2 ms delay introduced by the Arduino can be neglected for all gust cases, as it represents less than 2% of the gust period. However, the 50 ms delay required for the wingtip to react becomes significant for the high-frequency gusts. On the one hand, for the low-frequency gusts, 0.5 Hz, the delay remains below 5% of the gust period. On the other hand, for the high-frequency
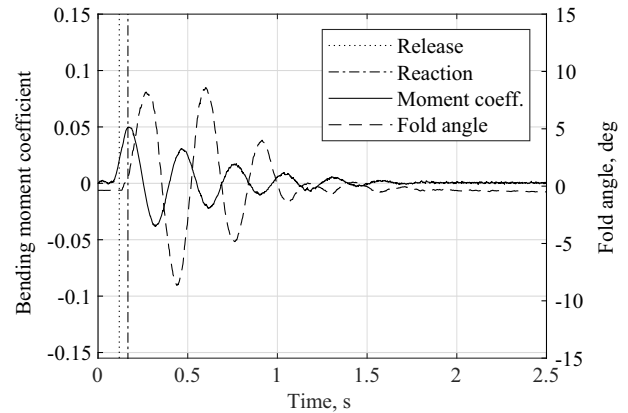

Fig. 18   Example of delay between actuator signal release and potentiometer response. Example of wing A, $\alpha = 0$ deg, 5 Hz gust, and 50% release.

Table 10   Comparison between gust periods and time delays introduced during the release

Gust		2 ms delay		50 ms delay	
Frequency, Hz	Period, ms	Reative delay, %	Phase delay, deg	Relative delay, %	Phase delay, deg
0.5	2000	0.1	0.4	2.5	9.0
1.5	667	0.3	1.1	7.5	27.0
3.0	333	0.6	2.2	15.0	54.0
3.5	286	0.7	2.5	17.5	63.0
5.0	200	1.0	3.6	25.0	90.0
8.0	125	1.6	5.8	40.0	144.0

gusts, this delay represents more than 20% of the gust period for the 5 and 8 Hz gusts. This can be seen in Fig. 19, where an example of time response at 0.5 Hz is compared to an example at 8 Hz. For the 0.5 Hz gust, when the hinge is released at 50% of the peak load, a 50 ms delay results in an effective release threshold of 60%, while the same delay at 8 Hz leads to an effective release threshold of 90%. Therefore, it is necessary to consider these delays when assessing the load alleviation performance of the wings.

2.   GLA Performance

The GLA performance of the FWT is assessed by comparing the peak loads and RMS with the performance of the wing in the locked-hinge configuration. First, the relative peak loads at $\alpha = 0$ deg are addressed to study the case in which no static load is applied. Then, the static load is included in the study of the peak loads at $\alpha = 5$ deg. Afterward, the introduction of oscillations is studied with the relative RMS. Similar to the peak loads investigation, first, the case in which

a) Bending moment time response for 0.5 Hz gust   b) Bending moment time response for 8 Hz gust

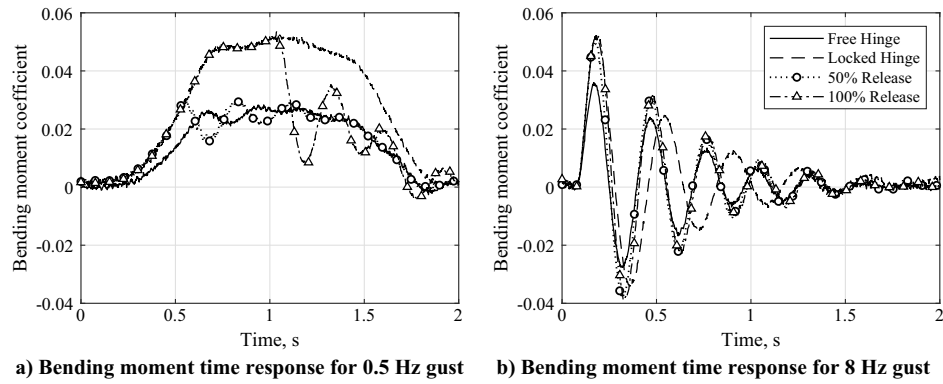Fig. 19 Comparison of time response for different release thresholds at different gust frequencies. Example from wing A at $\alpha = 0$ deg.

a) 0.5 Hz gust frequency

b) 1st flapping natural frequency, 1.5 Hz

c) 1st bending natural frequency, 3.0/3.5 Hz

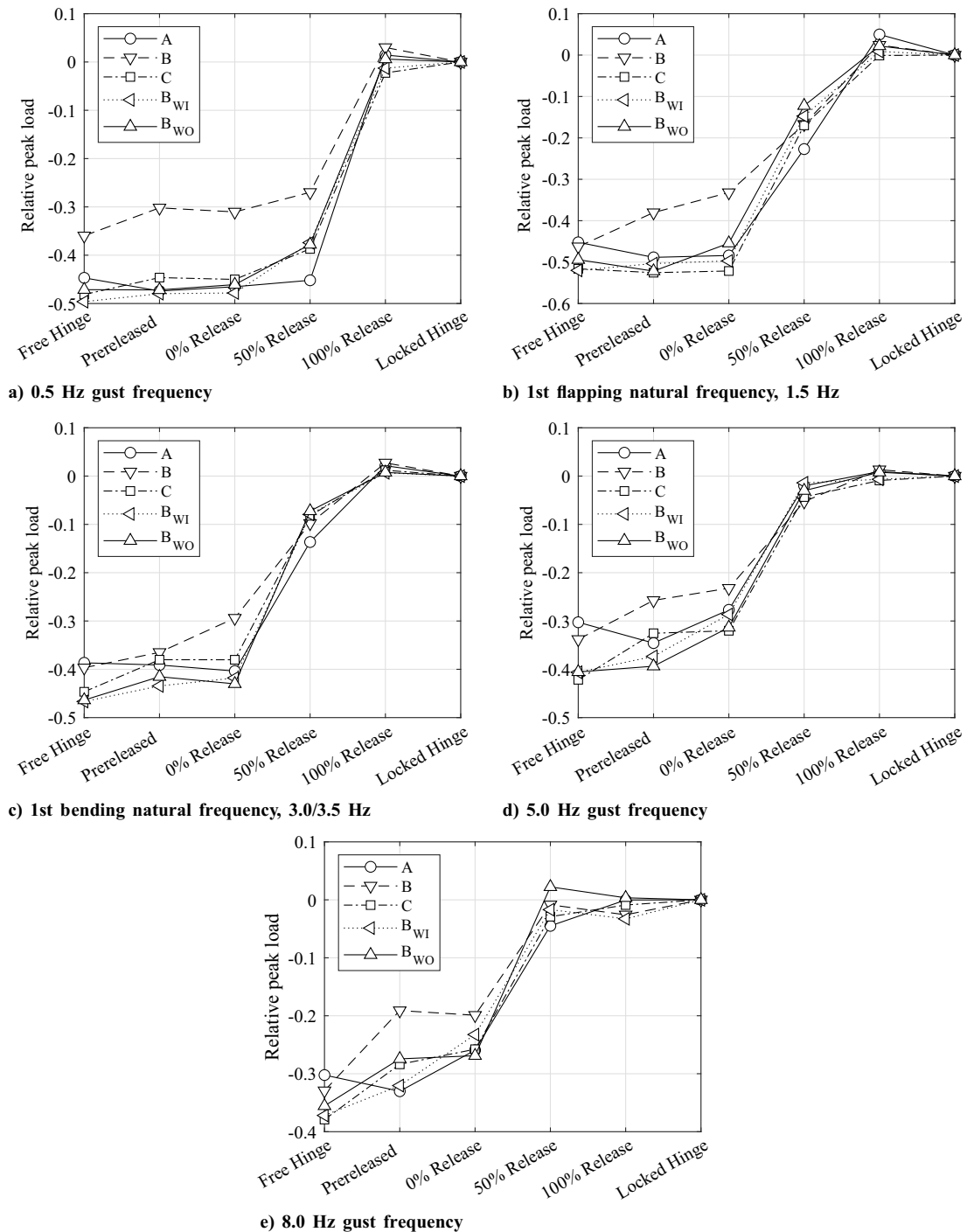d) 5.0 Hz gust frequency

e) 8.0 Hz gust frequency

Fig. 20 Relative peak load reduction with respect to peak load in locked-hinge condition for $\alpha = 0$ deg.

$\alpha = 0$ deg is addressed, and then the study is concluded with the $\alpha = 5$ deg case.

Figure 20 presents a comparison of the relative peak load alleviation between wings for different gust frequencies and release thresholds at $\alpha = 0$ deg. From these results, interesting remarks can be made regarding the release threshold and the peak loads when the hinge is released close to the peak load. First, the free-hinge condition can provide a peak load reduction between 30 and 50%, depending on the gust frequency and the wing stiffness. In agreement with the expectations, the peak load reduction is reduced with the delay in the release, as the wing is allowed to achieve higher loads before the hinge is released. Nevertheless, when the hinge is released at 100% of the peak load, the FWT can increase the peak loads with respect to the

locked-hinge condition. Notice also that this load increase depends on the gust frequency. For the 0.5 Hz gust, the peak increase can only be seen in the 100% release, while for the gust at 8 Hz, the load aggravation is also observed at 50% release. Furthermore, it can be seen how the load alleviation for the 50% release is progressively reduced with the increase of the gust frequency: for 0.5 Hz gust, the alleviation is similar to the free-hinge condition, while load aggravation can be observed for 8 Hz gusts. This change can be explained by the delays introduced by the release system, which significantly affect the effective load release threshold depending on the gust frequency. Therefore, the reduction in load alleviation seen with the increasing gust frequency is not caused only by the gust frequency but also by the change in the effective release threshold.

a) 0.5 Hz gust frequency

b) 1st flapping natural frequency, 1.5 Hz

c) 1st bending natural frequency, 3.0/3.5 Hz

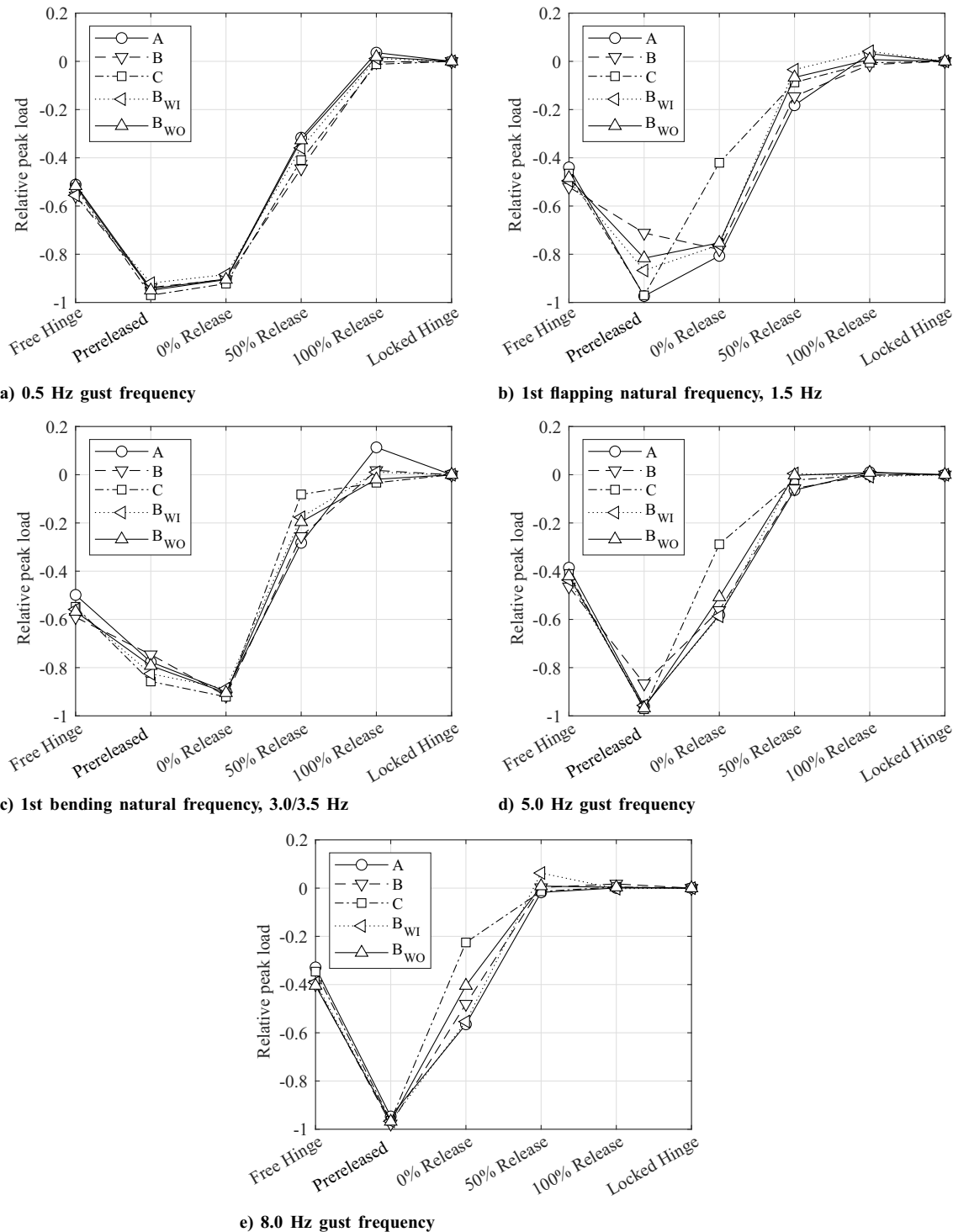d) 5.0 Hz gust frequency

e) 8.0 Hz gust frequency

Fig. 21   Relative peak load reduction with respect to peak load in locked-hinge condition for $\alpha = 5$ deg.

When comparing the different wings, wing B shows consistently lower load alleviation not only compared to the different stiffness wings, A and C, but also to the tailored wings, B_{WI} and B_{WO}. In addition, there is no significant difference between the tailored wings. Furthermore, exciting the wings at their natural frequencies does not seem to have an impact on the alleviation performance of the FWT. Even for wings B and C, which had the closest first bending natural frequencies to the excitation frequencies used in the test, the results do not stand out. Overall, the load alleviation capabilities are similar between wings for all gust frequencies.

Next, the case with the static aerodynamic loads is considered by increasing the angle of attack to $\alpha = 5$ deg. Figure 21 presents the respective comparison of the relative peak load reductions. Similar to the case without the static aerodynamic loads, the increase in peak loads still occurs for high-frequency gusts when the FWT is released beyond the 50% load threshold. However, there is an important difference when the hinge is prereleased and released at 0% of the peak load. The free-hinge condition allows for a peak load alleviation of about 45%, which is similar to the $\alpha = 0$ deg case. However, when the hinge is prereleased or released at the 0% load threshold, the peak load can be reduced even more, by up to 90%. To understand these results, Fig. 22a shows a comparison of the load response with a prereleased hinge and the respective response in locked-hinge and free-hinge conditions.

As seen in Sec. III.B.3, there is a difference between the steady state before the gust in the locked-hinge condition and after the gust hits, when the hinge has already been released. When the hinge is prereleased, the FWT starts moving toward the released equilibrium, reducing the load. Once the gust hits, the increase in load caused by the gust is compensated by the load relief caused by the movement that the FWT initiates when the hinge is released. As a result, the load barely increases above the initial steady load, leading to an almost 100% alleviation of the peak load.

This trend in the peak load reduction is observed for all the wings and gust frequencies. However, depending on the gust frequency, the peak load alleviation of the 0% release can be lower due to the release delays. Therefore, these results emphasize the importance of detecting the incoming gusts in advance, for example, using LiDAR-based detection [24]. Then, the prerelease instant can be optimized based on the gust length and trim attitude of the aircraft to maximize the gust load alleviation provided by the FWT.

To conclude the peak load assessment, the results at $\alpha = 5$ deg are similar to those at $\alpha = 0$ deg when looking at the effects of the different wing designs. This time, all the wings present a similar performance. Even though the peak reductions seen at $\alpha = 5$ deg are very promising, they are conditioned to a correct timing when releasing the hinge, because releasing at high load thresholds could aggravate the peak loads instead of alleviating them. In addition, there is an important drawback that cannot be seen from the relative peak loads. Figure 22b shows a gust response example in which,

together with a slight decrease in peak load, there is an important increase in the magnitude and persistence of the oscillation of the signal when the hinge is released. The RMS of the signals is used to study the impact of the release on the oscillations.

Figure 23 shows the relative RMS with respect to the locked-hinge condition at $\alpha = 0$ deg. Contrary to what has been seen for the peak load, not only does the hinge release affect the RMS, but also the wing stiffness and tailoring are important. On the one hand, the RMS behavior with respect to the hinge release is similar to that seen for the peak loads. When the hinge is free, the RMS reduction can vary between 20 and 55% depending on the wing and gust frequency. The RMS reduction decreases with the increasing release threshold, and, similarly to the peak loads, the oscillations can be aggravated with respect to the locked condition when the hinge is released at 100% of the peak load. For high-frequency gusts, this can also happen at 50% release. On the other hand, it is also possible to see differences between the wings for gusts at 1.5, 5, and 8 Hz. Wing A presents lower RMS reduction than wings B and C, while wing B presents the highest RMS reduction of all the wings. Both tailored wings, B_{WI} and B_{WO}, present lower RMS reduction than wing B, but wing B_{WO} achieves higher RMS reductions than B_{WI}. However, these trends cannot be observed for gust frequencies of 0.5 and 3/3.5 Hz corresponding to the first bending natural frequency. For these cases, the RMS reduction is similar between all the wings.

When the static aerodynamic load is included in the case of $\alpha = 5$ deg, three main remarks can be made from the results shown in Fig. 24. First, the trends observed at $\alpha = 0$ deg for the different wings in the 1.5, 5, and 8 Hz gusts can still be observed in this case, and this time, they also appear for the 0.5 Hz gust and the first bending natural frequency. Second, in contrast to the $\alpha = 0$ deg case, the excitation close to the first bending mode natural frequency has an impact on the RMS at $\alpha = 5$ deg. In this case, the RMS reduction is lower when the hinge is prereleased than when it is released at the 0% threshold. Last, the increase in RMS seen for hinge releases at 50 and 100% thresholds is amplified at $\alpha = 5$ deg and can also be seen for the 5 and 8 Hz gusts when released at 0% of the peak load. For these cases, the RMS can increase with respect to the locked-hinge condition by up to 150%, as in the example shown in Fig. 22b.

To conclude the discussion of the results, it has been seen that it is important to release the hinge instantly after the gust is detected, if not before. When the hinge is released close to the peak load, the load can not only be aggravated but also introduce significant oscillations, which tend to persist for a considerable amount of time after the gust has passed the wing. The introduction of these oscillations can be critical, as they can be considered detrimental for reasons such as fatigue of the wing structure or passenger comfort. However, the differences seen between the different wings show that it might be possible to minimize this impact with a proper structural design. In addition, other systems, like spoilers or the wingtip tab presented by
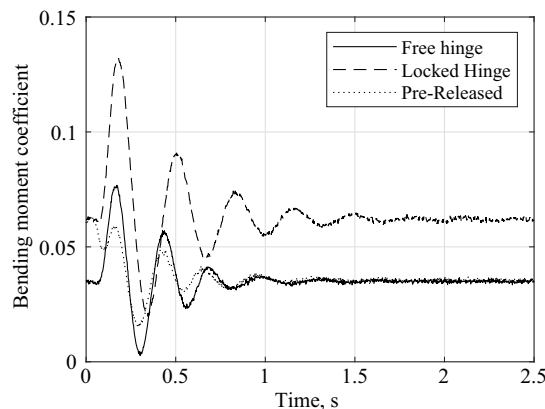
a) **Comparison of prerelease threshold with locked-hinge and free-hinge conditions at $\alpha = 5°$; example from wing B for 8 Hz gust**
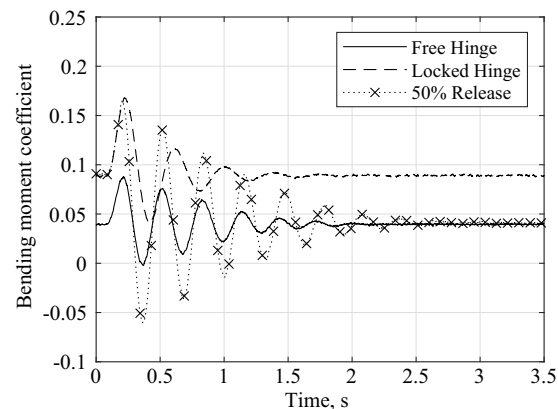
b) **Comparison of 50% threshold with locked-hinge and free-hinge conditions at $\alpha = 5°$; example from wing A for 5 Hz gust**

Fig. 22   Bending moment coefficient time response examples.

a) 0.5 Hz gust frequency

b) 1st flapping natural frequency, 1.5 Hz

c) 1st bending natural frequency, 3.0/3.5 Hz
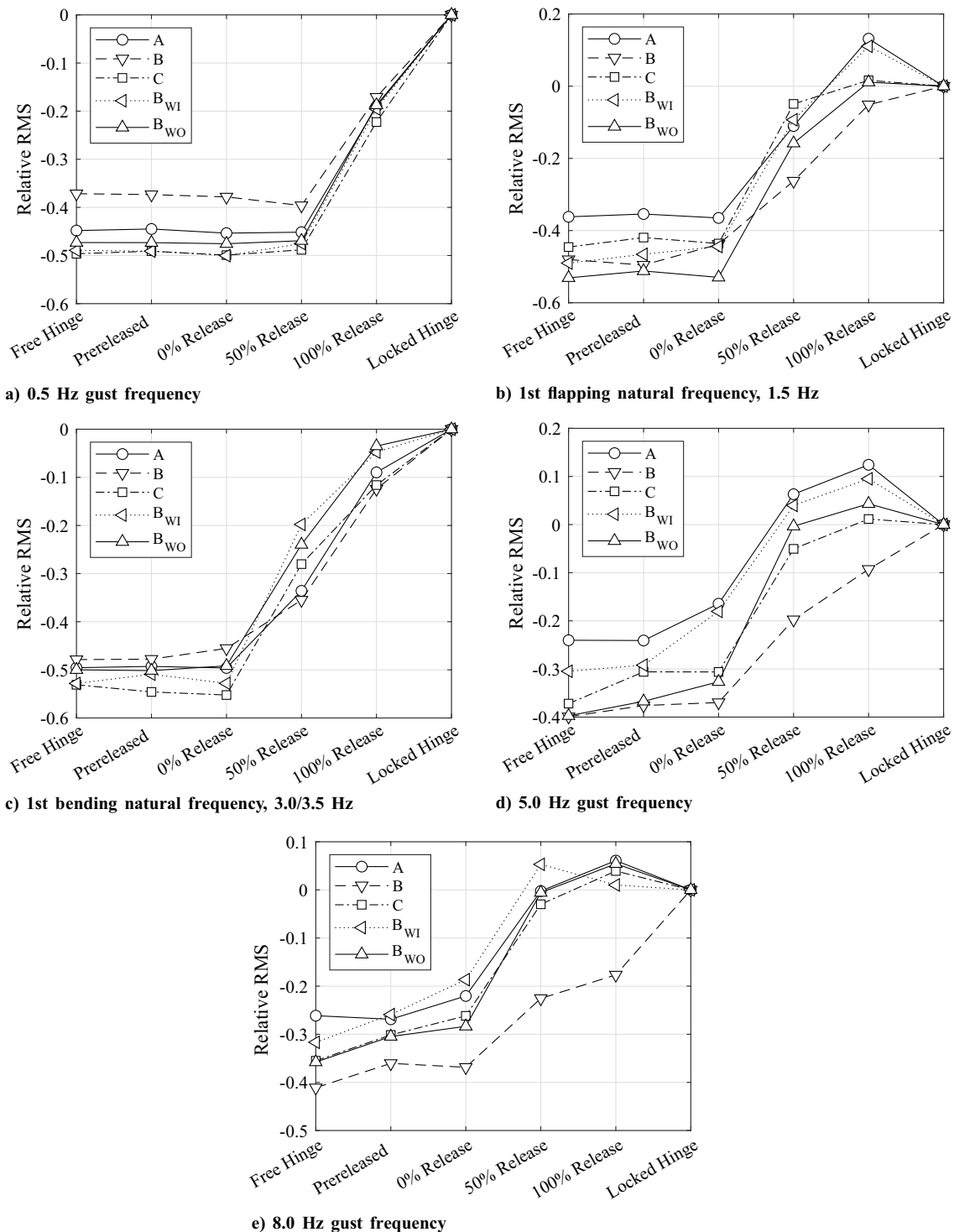
d) 5.0 Hz gust frequency

e) 8.0 Hz gust frequency

Fig. 23   Relative RMS reduction with respect to peak load in locked-hinge condition for $\alpha = 0$ deg.

Cheung et al. [6], could be combined to try to reduce these oscillations and further improve the GLA performance.
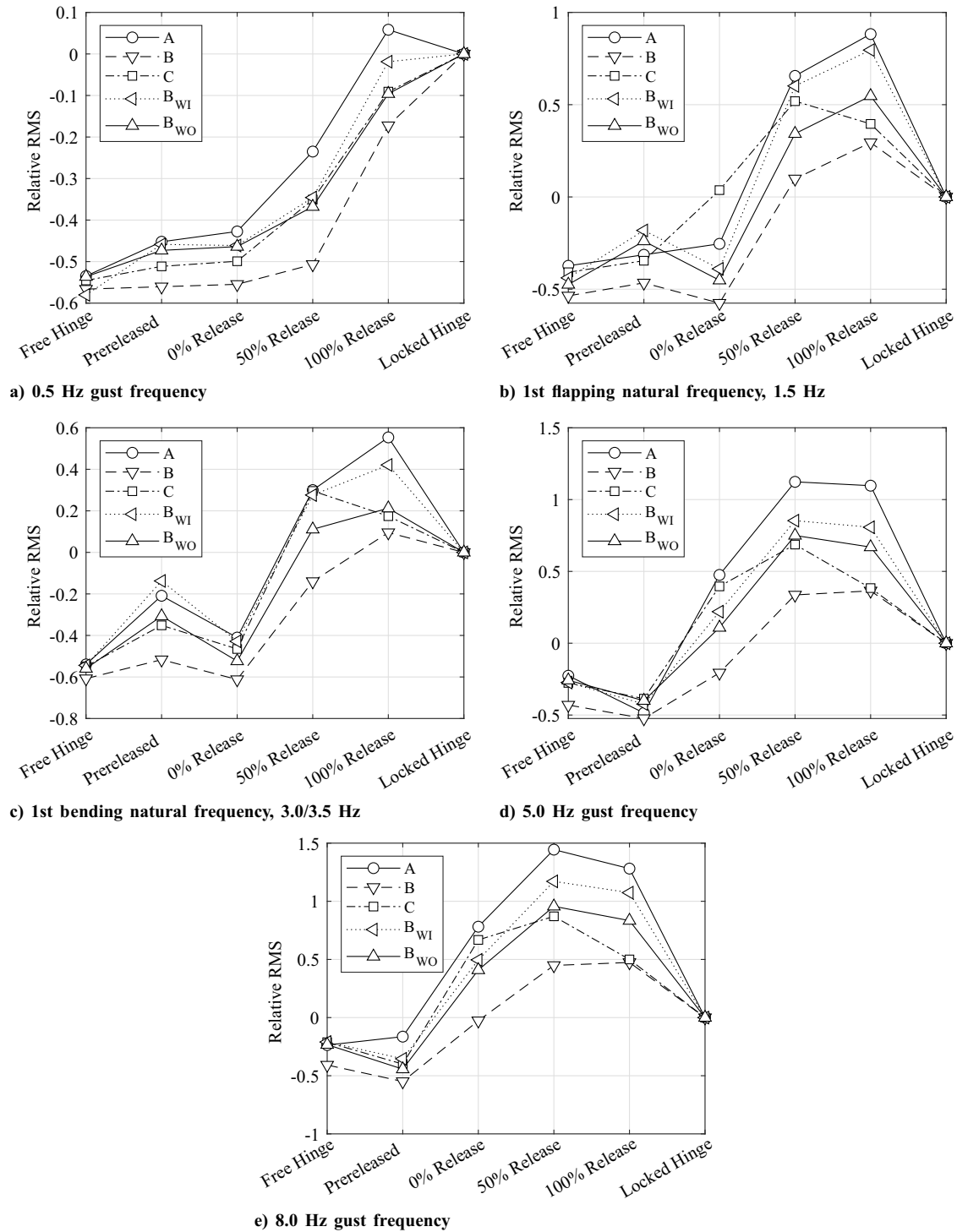
V.   Conclusions

This study presents the design and wind-tunnel investigation of a wing equipped with a flared folding wingtip, which can be released based on a specific load threshold. The wind-tunnel experiment was used to assess the effects of the bending stiffness and tailoring of the main wing as well as the impact of the hinge release instant on the final gust load alleviation of the folding wingtip.

It was found that the linear model used for the wing sizing overpredicts the flutter speed, between 5 and 34% depending on the stiffness

of the main wing. In addition, it was found that as the wingtip is released the flutter mechanism changes from first flapping/second flapping to second bending/first torsion, which leads to a considerable flutter speed reduction when the wingtip is released. Finally, the effect of tailoring on the flutter speed does not follow the conventional expectations reported in literature when the wingtip is operated in free-hinge condition: while wash-in tailoring would delay flutter in conventional wings, it promotes it when the folding wingtip is free to flap.

Considering static loads, the C_B polars show that the bending stiffness does not influence the static loads, leading to constant $C_{B,\alpha}$ across the stiffness range. On the other hand, tailoring affects the loads in an expected manner, with washout tailoring reducing and wash-in tailoring increasing the root bending moments.

a) 0.5 Hz gust frequency

b) 1st flapping natural frequency, 1.5 Hz

c) 1st bending natural frequency, 3.0/3.5 Hz

d) 5.0 Hz gust frequency

e) 8.0 Hz gust frequency

Fig. 24   Relative RMS reduction with respect to peak load in locked-hinge condition for $\alpha = 5$ deg.

Considering the dynamic loads, no clear relationship was observed between the peak load alleviation and the structural properties of the wing. On the other hand, there is a clear effect of the hinge release timing on the load alleviation. For statically unloaded conditions, corresponding to $\alpha = 0$ deg, releasing the hinge before the gust hits the wing is as effective as a released hinge. However, the later it is released, the worse the load alleviation becomes, even increasing the peak loads when it is released close to the peak load. When there is a static load, as in the case of $\alpha = 5$ deg, there is a significant difference in whether the hinge is released on time or not. When the hinge is prereleased, the gust peak load is reduced by more than 90%.

Although the dynamic release can alleviate the peak loads, it tends to increase the persistence of the wing oscillations induced by the gust, which can be considered detrimental for reasons such as fatigue of the wing structure or passenger comfort. For $\alpha = 0$ deg and the hinge releases close to the maximum load, these oscillations can become higher in amplitude and more persistent than if the hinge remained locked. For $\alpha = 5$ deg, this effect is magnified, leading to increments in the RMS values of more than 100% with respect to the locked-hinge condition.

These results emphasize the importance of detecting the gusts and being able to react on time. If the aircraft can detect them in advance and release the hinge before they hit the wing, the tradeoff between peak load reduction and oscillations can be positive. However, if the gust can only be detected when it hits the wing, the release and reaction time of the system needs to be short enough to avoid entering
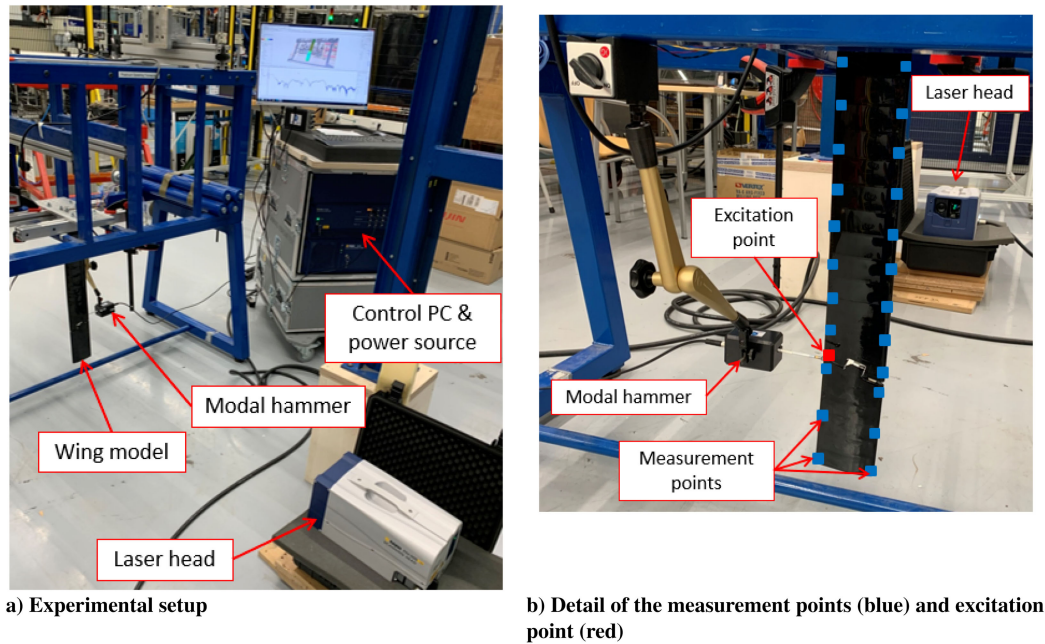
a) Experimental setup

b) Detail of the measurement points (blue) and excitation point (red)

Fig. A1   Overview of the ground vibration test setup.

the *late release* region for which the loads and the persistence of the gust-induced oscillations can be worsened.

To conclude, the present results open opportunities for future work on the flared folding wingtips. First, the differences in the predicted and measured flutter velocities in the free-hinge condition must be investigated to better understand the impact that releasing the hinge has on the stability of the wing. Second, a nonlinear aeroelastic model must be developed to better account for large wingtip deflections and the relation between the fold angle and the angle of attack of the wingtip. In addition, such a model would allow investigating the effect of the wingtip mass and the flare angle on the gust load alleviation capabilities and the release timing. Finally, focusing on the increased persistence of the oscillations, the combination of the folding wingtip with other means of gust load alleviation, such as ailerons or spoilers, can be investigated to reduce the oscillations and further reduce the peak loads.

The experimental data presented in this article will be made available in a data archive inside the collection of the 4TU.ResearchData center that can be found under at https://doi.org/10.4121/c.6070238.

Appendix A: Structural Characterization

To conclude the design of the wing model and the wind-tunnel experiment, this Appendix presents the correlation of the structural model with the results of ground vibration tests (GVT) to quantify the agreement of the model with the modal response of the wings. Afterward, the numerical model is updated with the objective of maximizing this correlation.

A.1.   Ground Vibration Tests

GVTs were conducted on the wings to correlate their natural frequencies and mode shapes with those obtained from the simulations. The GVT measurements were conducted with a Polytec PSV-500 laser scanning vibrometer[††††] and postprocessed with Simcenter TestLab. An overview of the test setup is presented in Fig. A1a. The wing was excited with a Maul-Theet vImpact-61 automatic modal hammer,[‡‡‡‡] which automatically hit the wing at a point on the trailing

---

[††††]See PSV-500 Scanning Vibrometer. Polytec, 2022, https://www.polytec.com/us/vibrometry/products/full-field-vibrometers/psv-500-scanning-vibrometer [retrieved 25 January 2022].

[‡‡‡‡]See Maul-Theet vImpact-61. Maul-Theet, 2020, https://www.maul-theet.com/wp-content/uploads/2020/09/en_MTn_vImpact_61_03.pdf [retrieved 25 January 2022].

edge close to the hinge axis (red dot in Fig. A1b). Furthermore, the vibration data was acquired from 24 points on the wing (blue dots in Fig. A1b) and averaged over ten different measurements. Finally, the data obtained from the GVTs was correlated to the FEM using the Model Correlation tool in Simcenter 3D, using the modal assurance criterion (MAC) to quantify the agreement between their mode shapes [25].

As a side note, the free-hinge configuration was tested for one of the wings, but it was found that the excitation provided by the modal hammer was not sufficient to be properly transferred to the wingtip due to the damping at the hinge. Therefore, the results obtained from the test were noisy and inconsistent; hence, only the results obtained from the tests in the locked-hinge configuration could be used.
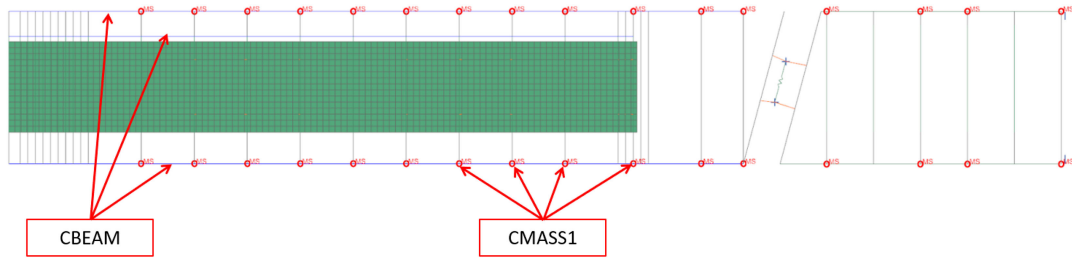
A.2.   Model Update

The model update procedure applied to improve the correlation with the experimental results is based on the work presented by Patelli et al. [26]. In this study, mass and stiffness elements were introduced in the model to account for uncertainties of the physical model, such as the stiffness of the joints or nonstructural mass elements. Afterward, these elements were optimized to increase the MAC values and reduce the frequency difference between the numerical model and the physical one.

Similarly, CBEAM and CMASS1 elements have been introduced in the FWT model to update the stiffness and mass properties, respectively. On the one hand, 50 beam elements of constant section and zero density have been added at the leading edge, trailing edge, and at the bottom and top surfaces at approximately the quarter-chord. These elements have a variable young modulus E with which the stiffness of the model can be increased without changing the mass distribution. On the other hand, 32 mass elements have been distributed along the leading and trailing edges to account for the mass distribution uncertainties. An overview of these elements can be found in Fig. A2.

Finally, the model update has been carried out using the FE Model Update add-on within the Simcenter 3D Model Correlation tool, which uses Nastran's SOL 200 to update the model based on the correlation results. Therefore, the added mass and stiffness elements are optimized to reduce the differences between the simulated modal frequencies and the GVT results as well as maximize the MAC values.

Fig. A2 Detail of the elements introduced in the FEM for the model updated. Mass elements represented as red dots and beam elements represented as blue lines.

A.3. Correlation Between Simulations and GVT Results

The comparison between the results from the GVT and the numerical results from the FEM is presented in Tables A1–A5. Looking at the results of the FEM before the update, the high MAC values indicate good agreement between the mode shapes [25], which can also be observed in Fig. A3. There, it is possible to see how the beam structure representing the GVT results presents the same shapes as the FEM mesh, especially for the first three modes, corresponding to the highest MAC values. Furthermore, there is agreement in the natural frequencies of the modes. For the first bending and first

torsion modes, the differences in the natural frequencies are below $\pm 10\%$, while for the second and third bending modes, the results show differences of up to 20%. However, the second torsion mode is clearly underpredicted with frequencies more than 40% lower than the GVT results. In addition, the trends predicted by the FEM simulation agree with the GVT in all the modes but the third bending mode: while the FEM predicts an increase of the natural frequencies when increasing the bending stiffness, the GVT results show a decrease in the frequencies with the increasing stiffness. This behavior might be explained by the compliance of the hinge mechanism. Babu and Krishna [27] showed that the dynamics of a structure including a flexible joint depend not only on the flexibility of the joint but also on its position with respect to the mode shape. Applying this knowledge to the FWT, the compliance of the locking mechanism seen in Sec. IV.C could be considered a source of flexibility, which is not considered in the FEM simulation and could lead to the previously mentioned discrepancies.

Next, the model is updated to reduce the differences in the natural frequencies and, if possible, improve the MAC. It can be seen how the average relative difference is reduced by 2 to 7% from the original difference. On the one hand, for all of the wings, the difference in the first bending mode is increased, while it is reduced for the rest of the modes. On the other hand, the MAC values present small improvements, but the average remains similar to the correlation before the model update.

Table A1   Correlation of GVT and FEM results before (f_{FEM}) and after (f_{UP}) model update for wing A

	Wing A				
Mode	f_{GVT}, Hz	f_{FEM}, Hz	MAC, -	f_{UP}, Hz	MAC
First bending	2.82	2.91 (+3.2%)	0.99	3.05 (+8.3%)	0.99
Second bending	19.89	16.48 (−17.2%)	0.96	19.94 (+0.2%)	0.94
First torsion	32.57	30.55 (−6.2%)	0.99	30.86 (−5.3%)	0.99
Third bending	49.65	42.76 (−13.9%)	0.90	46.47 (−6.4%)	0.91
Second torsion	147.04	84.67 (−42.4%)	0.90	88.49 (−39.8%)	0.92
Average[a]	— —	— —(16.6%)	0.95	— —(12.0%)	0.95

[a]Average computed with magnitude of the relative difference.

Table A2   Correlation of GVT and FEM results before (f_{FEM}) and after (f_{UP}) model update for wing B

	Wing B				
Mode	f_{GVT}, Hz	f_{FEM}, Hz	MAC	f_{UP}, Hz	MAC
First bending	3.10	3.20 (+3.2%)	0.99	3.33 (+7.4%)	1.00
Second bending	20.38	17.25 (−15.4%)	0.97	20.34 (−0.2%)	0.97
First torsion	35.82	34.30 (−4.2%)	0.98	34.16 (−4.6%)	0.97
Third bending	47.71	44.57 (−6.6%)	0.89	47.68 (−0.1%)	0.90
Second torsion	152.89	87.63 (−42.7%)	0.91	100.29 (−34.4%)	0.92
Average[a]	— —	— —(14.4%)	0.95	— —(9.3%)	0.95

[a]Average computed with magnitude of the relative difference.

Table A4   Correlation of GVT and FEM results before (f_{FEM}) and after (f_{UP}) model update for wing B$_{\text{WI}}$

	Wing B$_{\text{WI}}$				
Mode	f_{GVT}, Hz	f_{FEM}, Hz	MAC	f_{UP}, Hz	MAC
First bending	3.25	3.28 (+1.0%)	0.99	3.46 (+6.5%)	1.00
Second bending	21.88	17.46 (−20.2%)	0.98	21.68 (−0.9%)	0.95
First torsion	37.59	34.13 (−9.2%)	0.98	35.24 (−6.2%)	0.97
Third bending	52.82	45.47 (−13.9%)	0.91	50.12 (−5.1%)	0.91
Second torsion	156.59	87.11 (−44.4%)	0.94	100.04 (−36.1%)	0.89
Average[a]	— —	— —(17.7%)	0.96	— —(11.0%)	0.94

[a]Average computed with magnitude of the relative difference.

Table A3   Correlation of GVT and FEM results before (f_{FEM}) and after (f_{UP}) model update for wing C

	Wing C				
Mode	f_{GVT}, Hz	f_{FEM}, Hz	MAC	f_{UP}, Hz	MAC
First bending	3.52	3.60 (+2.3%)	0.99	3.77 (+7.3%)	1.00
Second bending	21.50	18.13 (−15.7%)	0.98	21.14 (−1.7%)	0.98
First torsion	43.06	38.98 (−9.5%)	0.95	40.42 (−6.13%)	0.95
Third bending	47.46	46.82 (−1.3%)	0.68	49.08 (+3.4%)	0.67
Second torsion	157.82	91.21 (−42.2%)	0.85	100.60 (−36.3%)	0.94
Average[a]	— —	— —(14.2%)	0.89	— —(11.0%)	0.91

[a]Average computed with magnitude of the relative difference.

Table A5   Correlation of GVT and FEM results before (f_{FEM}) and after (f_{UP}) model update for wing B$_{\text{WO}}$

	Wing B$_{\text{WO}}$				
Mode	f_{GVT}, Hz	f_{FEM}, Hz	MAC	f_{UP}, Hz	MAC
First bending	3.25	3.27 (+0.7%)	0.99	3.31 (+1.9%)	1.00
Second bending	19.53	17.50 (−10.4%)	0.95	19.12 (−2.1%)	0.96
First torsion	37.64	34.35 (−8.7%)	0.97	34.04 (−9.5%)	0.98
Third bending	43.26	45.10 (−4.25%)	0.84	45.63 (−5.5%)	0.92
Second torsion	151.72	88.73 (−41.5%)	0.81	94.26 (−37.9%)	0.89
Average[a]	— —	— —(13.1%)	0.91	— —(11.4%)	0.95

[a]Average computed with magnitude of the relative difference.

a) 1st bending mode   b) 2nd bending mode   c) 1st torsion mode

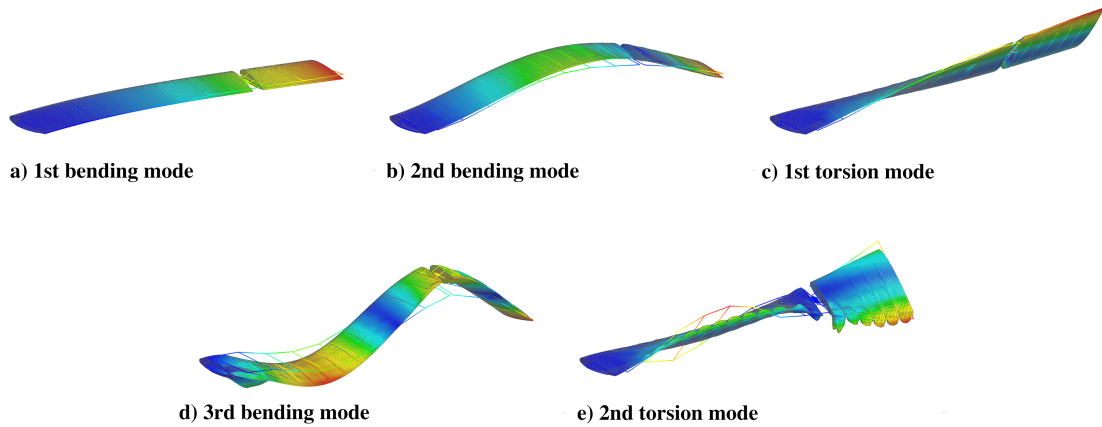d) 3rd bending mode   e) 2nd torsion mode

Fig. A3   Correlation of GVT mode shapes with FEM mode shapes.

References

[1] Anderson, J. D., *Fundamentals of Aerodynamics*, 6th ed., McGraw–Hill, New York, 2017, pp. 450–465.

[2] Smith, M. H., Renzelmann, M. E., and Marx, A. D., U.S. Patent Application for "Folding Wing-Tip System," The Boeing Company, Seattle, Washington, Docket No. 5,381,986 A, filed 17 Jan. 1995, https://worldwide.espacenet.com/patent/search?q=pn%3DUS5381986A [retrieved 1 July 2022].

[3] Wilson, T., Herring, M., Pattinson, J., Cooper, J., Castrichini, A., Ajaj, R., and Dhoru, H., International Patent Application for "An Aircraft Wing with Moveable Wing Tip Device for Load Alleviation," Airbus Operations Ltd., Bristol, Great Britain, U. K., Airbus Group Ltd., London, Great Britain, U. K., No. WO2017/118832Al, filed 13 July 2017, https://worldwide.espacenet.com/patent/search?q=pn%3DWO2017118832A1 [retrieved 1 July 2022].

[4] Castrichini, A., Siddaramaiah, V. H., Calderon, D., Cooper, J., Wilson, T., and Lemmens, Y., "Preliminary Investigation of Use of Flexible Folding Wing Tips for Static and Dynamic Load Alleviation," *Aeronautical Journal*, Vol. 121, No. 1235, 2017, p. 73–94.
https://doi.org/10.1017/aer.2016.108

[5] Cheung, R., Rezgui, D., Cooper, J., and Wilson, T., "Testing of a Hinged Wingtip Device for Gust Loads Alleviation," *Journal of Aircraft*, Vol. 55, No. 5, 2018, pp. 20–18.
https://doi.org/10.2514/1.C034811

[6] Cheung, R., Rezgui, D., Cooper, J., and Wilson, T., "Testing of Folding Wingtip for Gust Load Alleviation of Flexible High-Aspect-Ratio Wing," *Journal of Aircraft*, Vol. 57, No. 5, 2020, pp. 876–888.
https://doi.org/10.2514/1.C035732

[7] Castrichini, A., Hodigere Siddaramaiah, V., Calderon, D., Cooper, J., Wilson, T., and Lemmens, Y., "Nonlinear Folding Wing Tips for Gust Loads Alleviation," *Journal of Aircraft*, Vol. 53, No. 5, 2016, pp. 1391–1399.
https://doi.org/10.2514/1.C033474

[8] Castrichini, A., Wilson, T., and Cooper, J., "On the Dynamic Release of the Semi Aeroelastic Wing-Tip Hinge Device," *6th RAeS Aircraft Structural Design Conference*, Royal Aeronautical Society, 2018.

[9] Dussart, G., Yusuf, S., and Lone, M., "Identification of In-Flight Wingtip Folding Effects on the Roll Characteristics of a Flexible Aircraft," *Aerospace*, Vol. 6, No. 6, 2019, p. 63.
https://doi.org/10.3390/aerospace6060063

[10] Castrichini, A., Wilson, T., Saltari, F., Mastroddi, F., Viceconti, N., and Cooper, J. E., "Aeroelastics Flight Dynamics Coupling Effects of the Semi-Aeroelastic Hinge Device," *Journal of Aircraft*, Vol. 57, No. 2, 2020, pp. 333–341.
https://doi.org/10.2514/1.C035602

[11] Healy, F., Cheung, R., Neofet, T., Lowenberg, M., Rezgui, D., Cooper, J., Castrichini, A., and Wilson, T., "Folding Wingtips for Improved Roll Performance," *AIAA Scitech 2021 Forum*, AIAA Paper 2021-1153, 2021.
https://doi.org/10.2514/6.2021-1153

[12] Wilson, T., Kirk, J., Hobday, J., and Castrichini, A., "Small Scale Flying Demonstration of Semi Aeroelastic Hinged Wing Tips," *19th International Forum on Aeroelasticity and Structural Dynamics (IFASD 2019)*, Vol. 1, Curran Associates Inc., Red Hook, NY, 2019, pp. 1115–1133.

[13] Weisshaar, T., "Aeroelastic Tailoring—Creative Uses of Unusual Materials," *28th Structures, Structural Dynamics and Materials Conference*, AIAA Paper 1987-0976, 1987.
https://doi.org/10.2514/6.1987-976

[14] Avin, O., Raveh, D., Drachinsky, A., Ben-Shmuel, Y., and Tur, M., "An Experimental Benchmark of a Very Flexible Wing," *AIAA Scitech 2021 Forum*, AIAA Paper 2021-1709, 2021.
https://doi.org/10.2514/6.2021-1709

[15] "Simcenter 3D," Software Version 2020.1, Siemens PLM Software, Plano, TX, 2021. https://www.plm.automation.siemens.com/global/en/products/simcenter/simcenter-3d.html [retrieved 25 May 2021].

[16] "MSc Nastran," Software Version 2020, MSc Software, Hexagon AB, Stockholm, Sweden, 2021, https://www.mscsoftware.com/product/msc-nastran [retrieved 25 May 2021].

[17] Kassapoglou, C., *Review of Classical Laminated Plate Theory*, Wiley, Hoboken, NJ, 2013, pp. 33–53, Chap. 3.
https://doi.org/10.1002/9781118536933.ch3

[18] "Global Optimization Toolbox," Software Package, Mathworks, Natick, MA, R2021a, 2022, https://www.mathworks.com/products/global-optimization.html [retrieved 1 July 2022].

[19] Dillinger, J. K. S., Klimmek, T., Abdalla, M. M., and Gürdal, Z., "Stiffness Optimization of Composite Wings with Aeroelastic Constraints," *Journal of Aircraft*, Vol. 50, No. 4, 2013, pp. 1159–1168.
https://doi.org/10.2514/1.C032084

[20] Berkelman, P. J., Whitcomb, L. L., Taylor, R. H., and Jensen, P., "A Miniature Microsurgical Instrument Tip Force Sensor for Enhanced Force Feedback During Robot-Assisted Manipulation," *IEEE Transactions on Robotics and Automation*, Vol. 19, No. 5, 2003, pp. 917–921.
https://doi.org/10.1109/TRA.2003.817526

[21] Joo, J. W., Na, K. S., and Kang, D. I., "Design and Evaluation of a Six-Component Load Cell," *Measurement*, Vol. 32, No. 2, 2002, pp. 125–133.
https://doi.org/10.1016/S0263-2241(02)00002-7

[22] Tang, D. H., and Dowell, E. H., "Effects of Geometric Structural Nonlinearity on Flutter and Limit Cycle Oscillations of High-Aspect-Ratio Wings," *Journal of Fluids and Structures*, Vol. 19, No. 3, 2004, pp. 291–306.
https://doi.org/10.1016/j.jfluidstructs.2003.10.007

[23] Drachinsky, A., Avin, O., Raveh, D. E., Ben-Shmuel, Y., and Tur, M., "Flutter Tests of the Pazy Wing," *AIAA Journal*, Vol. 60, No. 9, 2022, pp. 5414–5421.
https://doi.org/10.2514/1.J061717

[24] Cavaliere, D., Fezans, N., Kiehn, D., Quero, D., and Vrancken, P., "Gust Load Control Design Challenge Including Lidar Wind Measurements and Based on the Common Research Model," AIAA Paper 2022-1934, 2022.
https://doi.org/10.2514/6.2022-1934

[25] Pástor, M., Binda, M., and Hararik, T., "Modal Assurance Criterion," *Procedia Engineering*, Vol. 48, Jan. 2012, pp. 543–548.
https://doi.org/10.1016/j.proeng.2012.09.551

[26] Patelli, E., Govers, Y., Broggi, M., Gomes, H. M., Link, M., and Mottershead, J. E., "Sensitivity or Bayesian Model Updating: A Comparison of Techniques Using the DLR AIRMOD Test Data," *Archive of Applied Mechanics*, Vol. 87, May 2017, pp. 905–925.
https://doi.org/10.1007/s00419-017-1233-1

[27] Gunda, J. B., and Krishna, Y., "Influence of Joint Flexibility on Vibration Analysis of Free-Free Beams," *Nonlinear Engineering*, Vol. 3, No. 4, 2014, pp. 237–246.
https://doi.org/10.1515/nleng-2014-0012